Materials Today 88 (2025) 186–200

Contents lists available at ScienceDirect

Materials Today

journal homepage: www.elsevier.com/locate/mattod

Research

# Stimuli-responsive gyroid Scaffolds: hierarchical architecture and electric stimulation promote bone regeneration

Rafael R.A. Silva [a,b,c,*], Frederico Barbosa [d,e], Guilherme Ferreira [c], Carlos Ureña [c], Eduardo H. Backes [a], José M. Inácio [f], José A. Belo [f], Rui Igreja [c], João C. Silva [d,e,g], Luiz H.C. Mattoso [b], Elvira Fortunato [c], Henrique M.V. Almeida [c], Rodrigo Martins [c,*], Caio G. Otoni [a,h,*]

[a] Graduate Program in Materials Science and Engineering (PPGCEM), Federal University of São Carlos (UFSCar), Rod. Washington Luís, km 235, 13565-905 São Carlos, SP, Brazil
[b] Nanotechnology National Laboratory for Agriculture (LNNA), Embrapa Instrumentation, 13560-970 São Carlos, SP, Brazil
[c] CENIMAT/i3N, Department of Materials Science, NOVA School of Science and Technology, NOVA University Lisbon (NOVA FCT) and CEMOP/UNINOVA, Campus de Caparica 2829-516 Caparica, Portugal
[d] Department of Bioengineering and iBB-Institute for Bioengineering and Biosciences, Instituto Superior Técnico, Universidade de Lisboa, Av. Rovisco Pais, 1049-001 Lisboa, Portugal
[e] Associate Laboratory i4HB – Institute for Health and Bioeconomy, Instituto Superior Técnico, Universidade de Lisboa, Av. Rovisco Pais, 1049-001 Lisboa, Portugal
[f] Stem Cells and Development Laboratory, iNOVA4Health, NOVA Medical School, Faculdade de Ciências Médicas, Universidade NOVA de Lisboa, 1169-056 Lisbon, Portugal
[g] Department of Mechanical and Aerospace Engineering and PolitoBIOMed Lab, Politecnico di Torino, Corso Duca Degli Abruzzi, 24, Turin 10129, Italy
[h] Institute of Chemistry, University of Campinas (UNICAMP), Campinas, SP, Brazil

ARTICLE INFO

*Keywords:*
Bone tissue engineering
Stimuli-responsive systems
3D printing
Cell alignment
Electric field
Piezoelectric scaffolds
Gyroid structures

ABSTRACT

Osteoporotic fractures in older adults place a significant burden on healthcare systems due to prolonged healing times and escalating costs. Innovative approaches closely mimicking the human bone microenvironment are paramount for advancing bone tissue regeneration. This study leverages a sacrificial template methodology to develop hierarchical 3D porous gelatin-$NaNbO_3$@PDMS scaffolds with gyroid structures mimicking cancellous bone architecture, tailored for enhanced stimuli-responsive biological performance. Modulating porosity levels (~0%, 18 %, and 63 %) enables macro-to-micro pore transitions, highlighting how porosity and zero-curvature surfaces impact critical properties for bioactive scaffold applications. Under simulated physical activity pressures, lower scaffold porosity enhances structural integrity, mechanical stability, and damping capacity, driven by reduced thickness plastic deformation. Corona discharge poling generates electrically charged stimuli-responsive scaffolds, enhancing electric field intensity through charge trapping. Combined with ultrasound stimulation (50 and 250 $mW{\cdot}cm^{-2}$), it boosts metabolic activity, gene expression, and mineralization, increasing calcium deposition by up to 1200 % compared to unstimulated controls. Finite element analysis reveals that the 63 % porosity scaffolds generate a sixfold stronger electric field than its 18 % counterpart, enhancing stimuli-responsive cell alignment, with ultrasound stimulation boosting it by ~10 %. These discoveries in zero-curvature geometries and stimuli-responsive systems redefine bone regeneration strategies by mimicking bone anisotropy through electric field stimulation, offering transformative insights for advanced biomaterials in implants and physiotherapy.

* Corresponding authors at: Graduate Program in Materials Science and Engineering (PPGCEM), Federal University of São Carlos (UFSCar), Rod. Washington Luís, km 235, 13565-905 São Carlos, SP, Brazil (RRAS, CGO); Institute of Chemistry, University of Campinas (UNICAMP), Rua Monteiro Lobato, 270, 13083-862 Campinas, SP, Brazil (CGO); and CENIMAT/i3N, Department of Materials Science, NOVA School of Science and Technology, NOVA University of Lisbon (NOVA FCT), Campinas da Caparica, 2829-516 Caparica, Portugal.
*E-mail addresses:* rafaelras@estudante.ufscar.br (R.R.A. Silva), rfpm@fct.unl.pt (R. Martins), cgotoni@unicamp.br (C.G. Otoni).

https://doi.org/10.1016/j.mattod.2025.06.013
Received 19 March 2025; Received in revised form 1 June 2025; Accepted 8 June 2025
Available online 17 June 2025

## Introduction

Stimuli-responsive materials exhibit the remarkable ability to adapt and respond to external stimuli in a tunable manner, representing a significant advancement over non-responsive materials. To enhance and modulate scaffold responsiveness, bioactive scaffolds can be developed by electrically charging their surfaces, harnessing bioelectricity to accelerate bone repair. This promising yet underexplored approach in tissue engineering holds particular potential for treating non-union fractures that fail to heal spontaneously. These scaffolds accelerate bone regeneration and clinical outcomes by leveraging bioelectric mechanisms central to bone homeostasis, e.g., cell proliferation, extracellular matrix secretion, and remodelling [1–3]. Bone cells respond to mechanical and electrical stimuli via pathways involving calcium signaling, growth factor release, and remodeling, while electric fields facilitate ion movement across cell membranes to support bone formation [1–5]. While weak electric currents have been studied extensively in enhancing calcium entry and mineralization [4,6–8], the use of electric fields in stimuli-responsive scaffolds with hierarchical porosity, e.g., produced by ultrasound stimulation (US), remains largely untapped.

US offers a novel, non-invasive method to enhance bone regeneration through electrically charged scaffolds that promote tissue repair, cell growth, and wound healing. To achieve the desired bioactivity, scaffolds must replicate bone tissue by incorporating hierarchical pores with precisely controlled sizes and bioactive inorganic particles [9]. However, creating such complex pore structures is challenging, particularly when incorporating high inorganic content. Fused filament fabrication (FFF) often struggles with poor particle distribution and nozzle clogging, compromising scaffold quality. A sacrificial template approach in FFF addresses these limitations, enabling the fabrication of complex scaffolds, e.g., gyroid structures with interconnected pores. These gyroids, mimicking cancellous bone, exhibit hierarchical macro-to-micro pores and a high surface area-to-volume ratio, promoting cell attachment, proliferation, and nutrient transport [10–12]. Additionally, their triply periodic minimal surface (TPMS) structure provides smoothly curved surfaces resembling trabecular bone, with isotropic mechanical properties ensuring uniform responses to mechanical stimuli, such as US [13,14].

The design structure and porosity level play a crucial role not only in influencing the mechanical performance but also in promoting bone cell ingrowth, e.g., by facilitating cellular attachment, neovascularization, and nutrient transport. While, recent studies have advanced our understanding of how porosity and surface charge influence mineralization under dynamic mechanical conditions [15], their impact on electric field distribution and intensity within scaffold structures, particularly those with hierarchical interconnected sinuous pores, remains largely unexplored. Therefore, the key focus is on designing gyroid scaffolds with hierarchical pore structures at two extreme porosity levels – low (18 %) and high (63 %) – to evaluate the impact of electric field intensity on biological features, e.g., stem cell growth and differentiation. Additionally, considering the membrane that covers the outer surface of all bones, i.e., the periosteum, composed of collagen, a gelatin coating on the scaffold surface is also essential to mimic the membrane and closely replicate real-world conditions [15–18].

Furthermore, because bone exhibits piezoelectric properties, strongly affecting the biological tissue's state, there has been growing interest in utilizing piezoelectric materials for bone tissue engineering lately [4]. However, commonly used piezoelectric materials like lead zirconate titanate (PZT) and lead titanate ($PbTiO_3$) present toxicity concerns, limiting their biomedical applications [19,20]. To address this, sodium niobate ($NaNbO_3$) demonstrates potential as a piezoelectric material and modulator of the dielectric constant, offering a lead-free, cost-effective, and non-toxic alternative. $NaNbO_3$ enhances surface charge retention in scaffolds, enabling fine control over electric field intensity and interactions within the pores, while its mechanical strength reinforces structural integrity and its antibacterial properties lower infection risk, making it a promising material for stimuli-responsive bioactive scaffolds [21,22].

Although piezoelectric scaffolds polarized by conventional methods achieve higher degrees of polarization and electrical output, corona discharge polarization offers a more versatile approach by electrically charging the surface regardless of scaffold geometry. Unlike DC polarization, limited to micrometer-scale thickness, corona discharge enables the injection of electrical charges into scaffolds with geometry-independent dimensions. Corona discharge also eliminates the challenging deposition of electrodes in porous scaffolds. Moreover, it enhances biocompatibility by eliminating the need for dielectric media, e.g., oils and fluorocarbon fluids, thus preventing the introduction of potentially harmful and persistent substances used in conventional techniques. This is essential for bioactive scaffold implants, as they can absorb dielectric media, leading to contamination, altered surface properties, and compromised functionality, potentially triggering inflammatory responses or other adverse effects *in vivo*.

In this study, we address three key issues, namely: (i) designing stimuli-responsive scaffolds containing at least 30 wt% inorganic particles with high structural complexity to replicate cancellous bone characteristics; (ii) elucidating the interrelationship among mechanical, structural, electrical, and bioactive responses, focusing on how US intensity and hierarchical pore levels synergistically enhance biological outcomes; and (iii) demonstrating, for the first time, the influence of electric field alignment on bone cell organization within 3D bioactive scaffolds with zero-curvature surfaces, in contrast to traditional sharp-pore designs. Using a sacrificial template method, we fabricated high-quality $NaNbO_3$@PDMS scaffolds with tunable porosity, providing novel insights into the synergy between scaffold architecture, electrical stimulation, and mechanical performance in promoting bone cell regeneration. This work offers promising directions for next-generation bioactive scaffolds and innovative physiotherapy approaches in bone regenerative medicine.

## Results and discussion

### *Fabrication and biological assessment of Gyroidal bioactive scaffolds*

Developing composite scaffolds with high and uniformly distributed inorganic content within complex 3D geometries remains a critical challenge in tissue engineering. To address this, a gyroid-based sacrificial template was fabricated via 3D FFF printing using the acrylonitrile–butadiene–styrene (ABS) terpolymer, producing porosities of *ca.* 35 %, 80 %, and 100 % (Fig. 1**a1**). The gyroid architecture was strategically selected to mimic trabecular bone microarchitecture while ensuring isotropic mechanical behavior and uniform transmission of mechanical and electrical stimuli, particularly during ultrasound stimulation. Its continuous, zero-mean curvature pore network minimizes stress concentrations, promotes uniform acoustic wave propagation, and enhances mechano-electrical coupling throughout the 3D scaffold, supporting efficient and homogeneous cellular stimulation. In addition, to enhance dielectric properties and piezoelectric performance, 30 wt% $NaNbO_3$ was incorporated into the PDMS matrix, cast into the templates, thermally cured (Fig. 1**a2**), and immersed in chloroform to dissolve the ABS templates (Fig. 1**a3**), yielding porous scaffolds with confirmed porosities of ~ 0 %, 18 %, and 63 % as analyzed by X-ray μCT (Fig. 1**a4**).

Fig. 1**b** illustrates the protocol used to evaluate the bioactivity of the scaffolds, focusing on bioelectricity mechanisms stimulated by physiotherapy-like procedures, i.e., US. Two distinct US regimens were tested: low-US (50 $mW{\cdot}cm^{-2}$) and high-US (250 $mW{\cdot}cm^{-2}$), along with a non-stimulated control condition (0 $mW{\cdot}cm^{-2}$) (Fig. 2**b1**). Scaffolds were positioned using a custom-designed 3D-printed holder within a cell culture plate and subjected to stimulation for 3 min every other day over a 14-d culture period (Fig. 1**b2**).

Fig. 1**c** presents the experimental timeline for biological

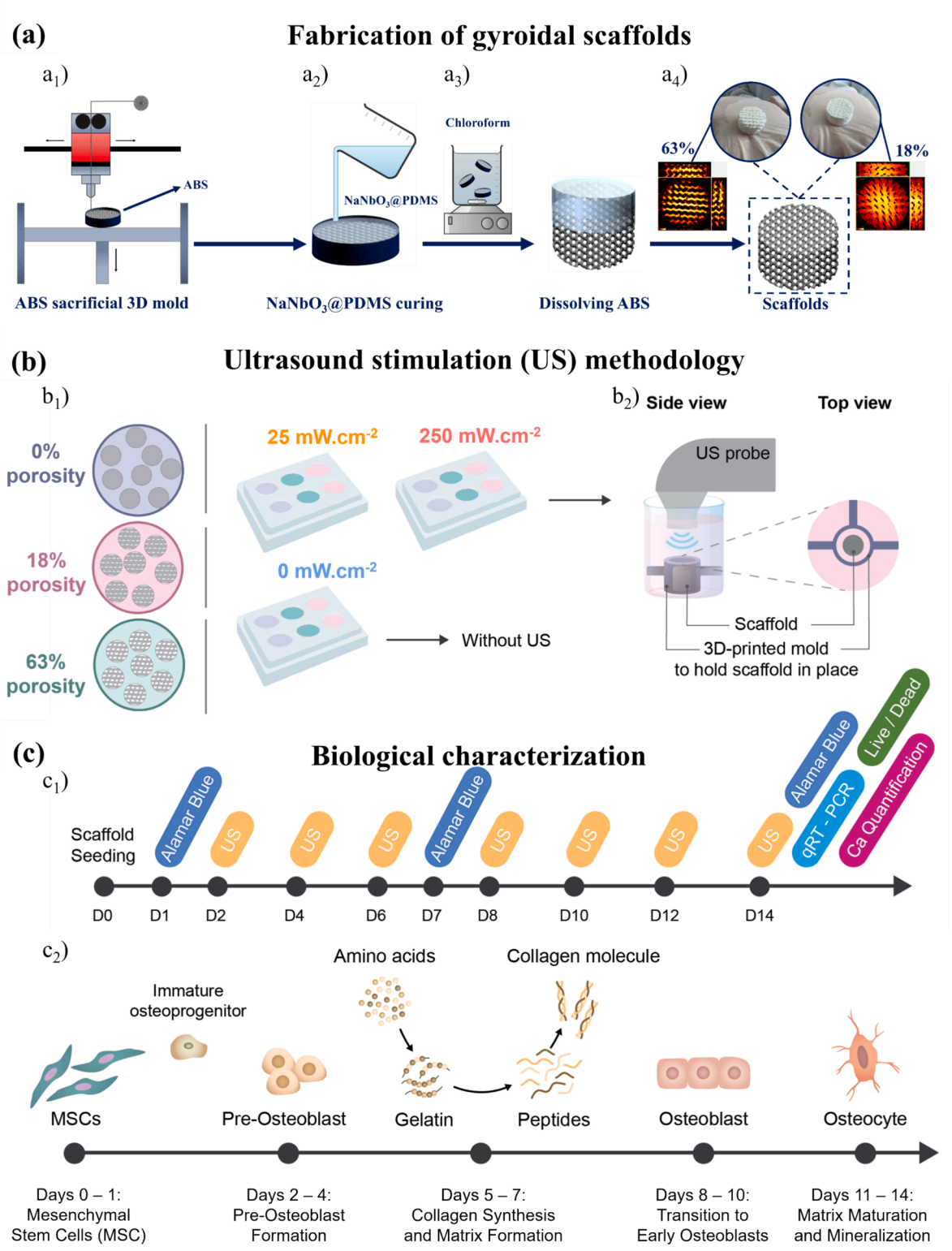


**Fig. 1.** Schematic illustration of the development of gyroid-based $NaNbO_3$@PDMS scaffolds with tunable porosity and their biological assessment for bone tissue regeneration. (a) Fabrication process: $a_1$) Sacrificial templates are created using a 3D fused filament fabrication (FFF) printer. $a_2$) $NaNbO_3$@PDMS composite is poured into the template and cured to form the scaffold structure. $a_3$) ABS sacrificial template is dissolved in chloroform. $a_4$) Final scaffolds with porosities of 0 %, 18 %, and 63 % are obtained, as quantified by X-ray microcomputed tomography. (b) Schematic representation of the ultrasound stimulation (US) methodology: $b_1$) Scaffolds with 0 %, 18 %, and 63 % porosities underwent US at intensities of 0, 50, and 250 mW·cm$^{-2}$ in 9-well plates. b2) Scaffolds were held in position using a custom 3D-printed model within a cell culture plate. Each well corresponded to a specific US condition, with the control condition representing non-stimulated samples. (c) Biological characterization timeline: $c_1$) Experimental timeline outlines scaffold seeding on 0 d, followed by 3-min US treatments every 2 d with bone cell growth monitored over 14 d. Alamar Blue assays were performed on days 1, 7, and 14, while qRT-PCR and calcium quantification assays were conducted on day 14 to assess cellular activity and mineralization. $c_2$) Stages of cellular growth and differentiation during osteogenesis: MSCs (Days 0–1) differentiate into pre-osteoblasts (Days 2–4). Collagen synthesis and matrix formation occur (Days 5–7), followed by transition to osteoblasts (Days 8–10). The matrix matures and mineralizes into osteocytes (Days 11–14). (For interpretation of the references to colour in this figure legend, the reader is referred to the web version of this article.)

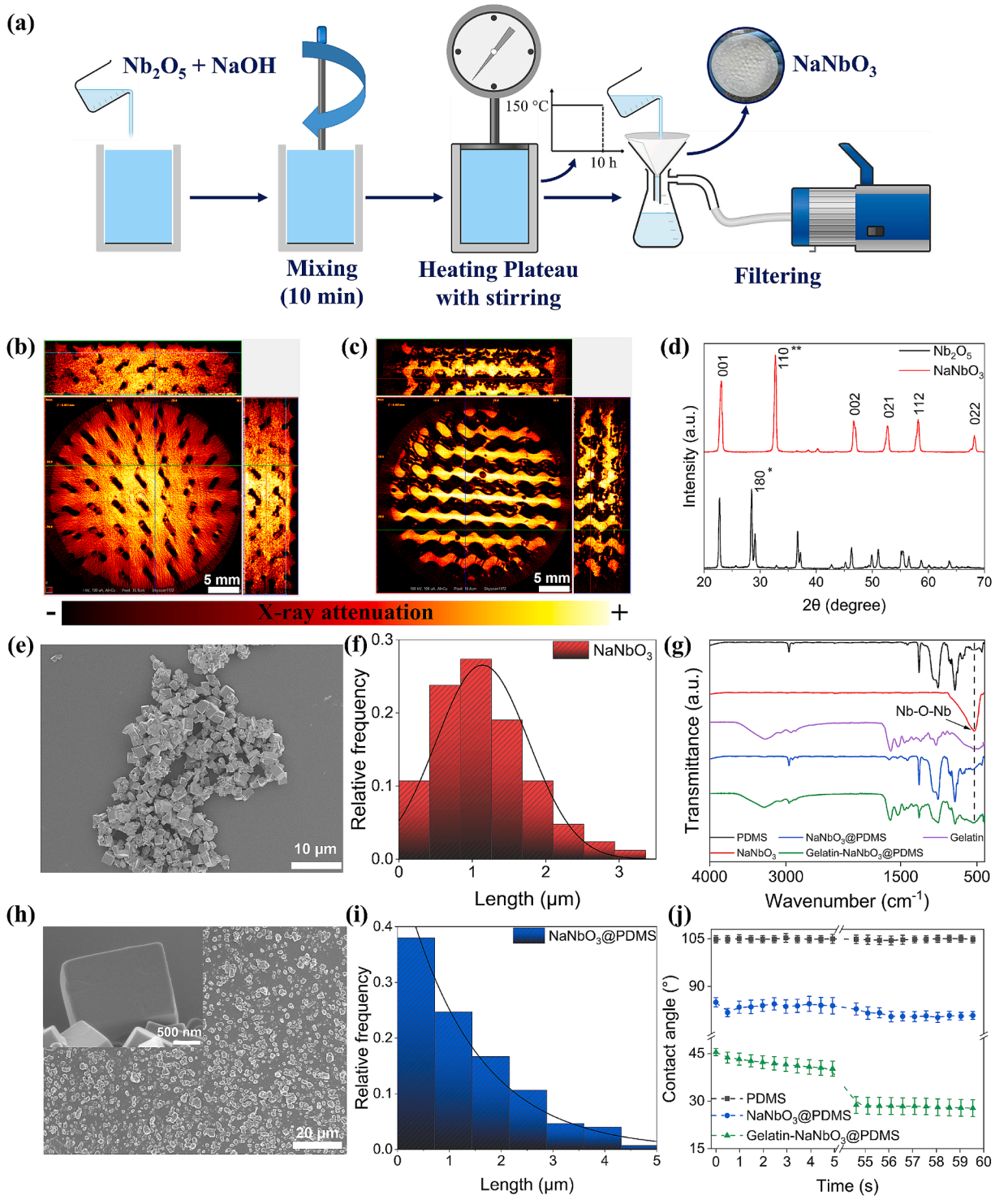


**Fig. 2.** Characterization of synthesized materials and gelatin-PDMS@$NaNbO_3$ scaffolds. (a) Schematic illustration of the hydrothermal synthesis approach for cubic $NaNbO_3$ particles, employing the reaction of $Nb_2O_5$ with NaOH (15 M) at 150 °C for 10 h, followed by filtration and drying to yield perovskite-phase $NaNbO_3$. X-ray microcomputed tomography reconstructions (top, frontal, and side views) of scaffolds with (b) 18 % and (c) 63 % porosity (scale bar = 5 mm). Lighter areas indicate higher X-ray attenuation. (d) XRD patterns of annealed $NaNbO_3$ nanoparticles: * marks the strongest $Nb_2O_5$ peak, and ** indicates the $NaNbO_3$ perovskite phase. (e) SEM images of $NaNbO_3$ at (f) 2 k magnification (scale bar = 10 μm) and (h, inset) 40 k magnification (scale bar = 500 nm), and (h) $NaNbO_3$@PDMS surface at 950× magnification (scale bar = 20 μm). Particle size distribution of synthesized (f) $NaNbO_3$ and (i) 30 wt% $NaNbO_3$ particles incorporated on the PDMS. (g) ATR-FTIR spectra of PDMS (black), $NaNbO_3$ (red), $NaNbO_3$@PDMS (blue), and gelatin-$NaNbO_3$@PDMS (green). (j) Contact angle measurements of PDMS (black), $NaNbO_3$@PDMS (red), and gelatin-$NaNbO_3$@PDMS (blue) over 60 s. (For interpretation of the references to colour in this figure legend, the reader is referred to the web version of this article.)

characterization, designed to assess the bioactivity of scaffolds in response to US. Scaffold seeding occurred on day 0, followed by 3-min US treatments every other day, with Alamar Blue assays measuring cell viability and metabolic activity on days 1, 7, and 14, and qRT-PCR and calcium quantification assessing gene expression and mineralization, respectively, on day 14 (Fig. 1**c1**). A framework for understanding the temporal effects of US on each stage of bone tissue formation is presented, aiding in the interpretation of experimental outcomes (Fig. 1**c2**). It illustrates the progression of cellular growth and differentiation during osteogenesis, beginning with mesenchymal stem cells (MSCs) on days 0–1, and transitioning to pre-osteoblasts by days 2–4. Collagen synthesis and matrix formation occur from days 5 to 7, followed by osteoblast development on days 8–10. By days 11–14, the matrix matures and mineralizes into osteocytes.

*Chemical and morphological characterization of gyroid scaffolds*

$NaNbO_3$ nanocubes were synthesized via a hydrothermal process with precise temperature control (Fig. 2**a**). 15 M NaOH solution was mixed with 1 g of $Nb_2O_5$ for 10 min, then transferred to a PTFE container, sealed with PTFE tape, and placed in a hydrothermal reactor. The temperature was raised at 10 °C·min$^{-1}$ to 150 °C and held for 10 h to enable nanocube formation. After rapid cooling in cold water, the precipitate ($6NaNbO_3{\cdot}2H_2O$) was washed with Milli-Q water to remove residual NaOH and vacuum-filtered to isolate $NaNbO_3$ nanoparticles. Since $NaNbO_3$ can form various polymorphs (e.g., orthorhombic, cubic, tetragonal), annealing at 600 °C for 12 h was performed to improve crystallinity and ensure phase purity, yielding perovskite $NaNbO_3$ nanocubes consistent with previous studies [23,24].

The $Nb_2O_5$ precursor exhibited an XRD peak at 28.5° (Fig. 2**d**), corresponding to pseudohexagonal $Nb_2O_5$ (JCPDS: 28–317) [25,26]. Additionally, six prominent peaks at 22.9, 32.5, 46.6, 52.5, 58.1, and 68.13° were identified, corresponding to the (001), (110), (002), (021), (112), and (022) planes of the orthorhombic $NaNbO_3$ phase [27–29]. The FTIR spectrum of the $NaNbO_3$@PDMS composite further confirmed the synthesis and crystalline structure of $NaNbO_3$, indicated by the band cantered at 536 cm$^{-1}$ for M−O stretching, M−O−M bending (M = Nb, Na), and lattice vibrations typical of the perovskite phase (Fig. 2**g**) [28,30,31]. This broad absorption band, along with the absence of the 1640 cm$^{-1}$ water-stretching signal, confirms the loss of hydrated water upon annealing of $NaNbO_3{\cdot}2H_2O$, while the absence of additional bands further validates the $NaNbO_3$ perovskite phase, consistent with XRD results. Furthermore, the coating of $NaNbO_3$@PDMS with gelatin confirmed the presence of O–H stretching at 3600 cm$^{-1}$, C=O stretching at 1637 cm$^{-1}$ (amide I), and N–H deformation between 1500 and 1550 cm$^{-1}$ (amide II) [32]. These bands contribute to surface hydrophilization of scaffolds and also serve as non-specific binding sites for cells.

X-ray μCT confirmed scaffold porosities of 18 % and 63 % after dissolving the ABS template (Fig. 2**b-c**, respectively). The slight difference in porosity (2 % less porous) between the experimentally determined porosity by X-ray μCT and the designed 3D model is attributed to thermal warping of ABS during 3D printing. A 60 % porosity level has been shown to facilitate neovascularization and bone ingrowth, facilitating oxygen and nutrient transport, essential for tissue regeneration [33–35]. Additionally, X-ray μCT movies highlight the exceptional conformability and shape fidelity of both scaffold structures after pouring and curing $NaNbO_3$@PDMS, with only a few minor bubbles (Supplementary Movie S1).

The $NaNbO_3$ particles had a predominantly cubic morphology, as revealed by SEM (Fig. 2**e, and 2h inset**). Using Scott's rule to determine the optimal bin width, a Gaussian curve was fitted to the relative frequency distribution of $NaNbO_3$ particle lengths, revealing a peak content (25 %) at 1 μm (Fig. 2**f**). Furthermore, after incorporating 30 wt% $NaNbO_3$ into PDMS, uniform distribution and dispersion of the particles were observed (Fig. 2**h**), with an exponential curve indicating a peak content (37 %) at the nanoscale, i.e., < 1 μm (Fig. 2**i**). Following the development of $NaNbO_3$@PDMS scaffolds, the gelatin coating was applied, resulting in a submicron-scale surface roughness that can promote enhanced cell attachment (**Supplementary Fig. S1c**).

Contact angle measurements confirmed the hydrophobic nature of the PDMS scaffold (105°) (Fig. 2**j**). After incorporating $NaNbO_3$, the contact angle significantly decreased to 86°, indicating a shift towards a hydrophilic surface (< 90°), attributed to the presence of hydrophilic groups (e.g., M−O). The gelatin coating further enhanced the wettability by water, with an initial contact angle of 45°, which steadily decreased to 26° within 60 s. This surface modification is crucial not only for promoting protein adsorption and cell adhesion through functional groups (e.g., amides) but also for forming a hydration layer that better mimics the aqueous conditions of the human body, thereby minimizing immunogenic reactions [36,37]. Furthermore, because gelatin is derived from collagen, the primary component of the extracellular matrix (ECM) in tissues, it helps to create a scaffold that closely resembles the natural bone microenvironment. This resemblance facilitates enhanced cell adhesion, cell–cell and cell-ECM interactions, and supports cellular growth and differentiation, thereby promoting tissue regeneration. This biomimetic scaffold allows for a more effective investigation of the interrelationship between porosity, US, and electric field intensity in gyroid-structured scaffolds.

*Structural features and stability work regimes*

The structural features of the bioactive scaffolds were characterized to confirm the quality of their hierarchical porous structures, focusing on porosity level, pore dimensions, and distribution of pores (Fig. 3). The sacrificial template 3D digital models for scaffolds, where the porous regions transform into solid sections following the incorporation of $NaNbO_3$@PDMS for 18 and 63 % porosity, are shown in Fig. 3**a-b**, respectively. High-resolution 3D X-ray μCT reconstructions validate the quality and integrity of the gyroid-structured scaffolds for both porosity levels, showcasing well-defined pores. Further corroboration is provided through digital images of scaffolds in their original dimensions, along with magnified views showing the scaffolds after resizing their diameters from 100 to 8 mm (**Fig. S1d-h**).

SEM reveals peripheral pore dimensions of 1.3 × 0.5 and 4.2 × 0.7 mm$^2$ for scaffolds with 18 and 63 % porosity, respectively. These results indicate that both scaffolds possess macro-scale peripheral pores, with major diameters of 1.3 and 4.2 mm, respectively. These features are conducive to fluid and nutrient exchange, while their minor diameters (*ca.* 500 μm) align with optimal pore sizes for supporting cell growth. Previous studies have shown that larger pore sizes, e.g., 800 μm, significantly enhance bone regeneration by providing sufficient space for cell ingrowth [38,39]. For instance, Montazerian et al. reported that magnesium scaffolds with larger pore sizes promote mature bone formation by promoting vascularization [40].

The trade-off between scaffold porosity and mechanical, functional, and biological properties is illustrated in Fig. 3**c**. Increasing porosity in scaffolds reduces material density, weakening mechanical stability but enhancing electric field intensity and biological recovery by facilitating electric field propagation through the pores. Lower porosity enhances mechanical stability by resisting deformation but diminishes electrical functionality and biological performance due to reduced dielectric shielding and smaller pore size. Mechanical stress further affects functionality, as low stress within the elastic regime preserves structural integrity but reduces stimuli-responsive effects for biological outcomes.

Preserving pore structural integrity is crucial for evaluating stimuli-responsive biological outcomes in scaffolds, ensuring bone cells are not stressed by pore wall compression under plastic deformation. The functional stability of the 63 % porosity scaffold, evaluated via $V_{oc}$ signal fluctuations under elastic (0.2 MPa) and plastic (3 MPa) stress conditions, showed a steady decline over 10,000 cycles (Fig. 3**d**). This decline likely reflects degradation of the top and bottom electrodes,

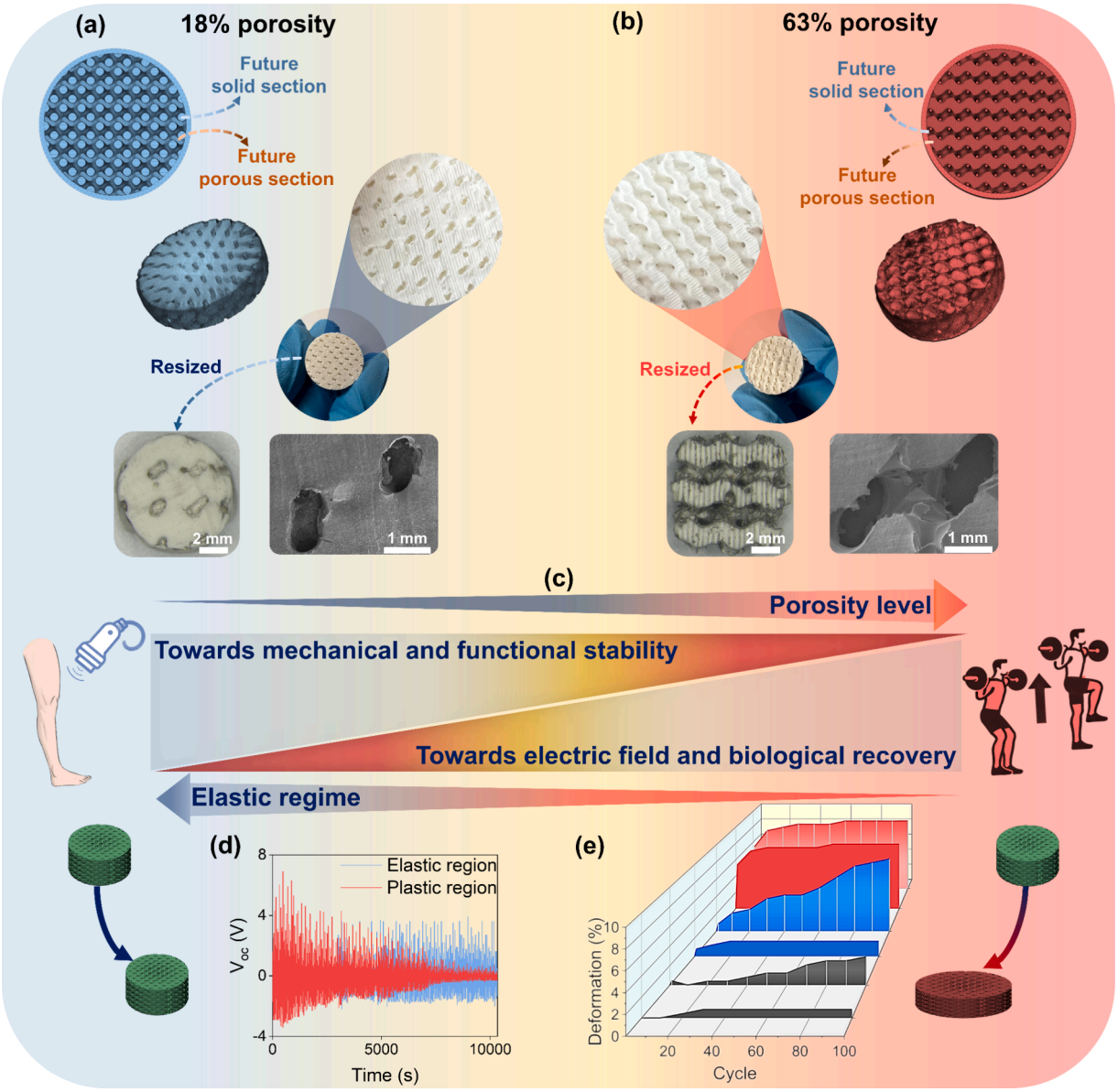


**Fig. 3.** Influence of scaffold porosity on structural organization, microarchitecture, mechanical behavior, and functional performance. Comparison of gyroid-based scaffolds with (a) low porosity (18 %) and (b) high porosity (63 %), highlighting differences in structural organization and pore distribution. The comparative analyses include 3D X-ray microcomputed tomography reconstructions, digital photographs of scaffolds (100 mm in thickness and 100 mm in diameter), stereo microscope views of resized scaffolds (scale bar = 2 mm), and SEM images of porous regions at 35× magnification (scale bar = 1 mm). (c) Trade-off diagram illustrating the interplay between porosity levels and mechanical stress regimes on mechanical stability and biological/electrical performance. (d) Open-circuit voltage ($V_{oc}$) signal fluctuations of 63 % porosity scaffold under elastic (0.2 MPa) and plastic (3 MPa) regimes across 10,000 cycles. (e) Progressive deformation (densification) of scaffold thickness under 12.5 % (darker curves) and 50 % strain (lighter curves, hatched with vertical lines) over 100 cycles for scaffolds with 0 % (black), 18 % (blue), and 63 % (red) porosity. Green scaffolds indicate pristine structural integrity, whereas red highlights thickness-compression deformation under mechanical stress in the plastic regime. (For interpretation of the references to colour in this figure legend, the reader is referred to the web version of this article.)

disrupting the conductivity network and reducing electrical output. The degradation results from mismatched plastic deformation between scaffold materials, with yield stress points of *ca.* 2 MPa for PDMS and 200 MPa for the Au/Pd electrodes, leading to inevitable surface cracking and compromised electrical connectivity over prolonged cycles.

Assessing thickness deformation is vital for evaluating scaffold stability over extended cycles and identifying stress–strain ranges that mechanically activate scaffolds without overstressing cells and compromising structural integrity. Thickness deformation correlates positively with porosity and strain; as both increase, so does the deformation (Fig. 3**e**). Scaffolds with 63 % porosity exhibit significant degradation after the second cycle, with ~ 8 % thickness deformation, regardless of applied strain, indicating lower structural stability and higher densification rates. In contrast, 0 and 18 % porosity scaffolds show minimal densification (~1.5 %) at 12.5 % strain but experience progressive deformation at 50 % strain. Therefore, higher mechanical stress (e.g., 3 MPa in the plastic regime) further affects scaffold functional stability via thickness deformation. These findings highlight the need for lower-stress stimuli, such as US, to preserve pore structure and scaffold integrity while reducing stress on bone cells.

Densification strain increases with porosity, reaching *ca.* 40 %, 45 %, and 49 % as porosity increases from 0 % to 18 % and 63 %, respectively (**Table S1**). This underscores the importance of limiting applied stress, with mechanical compression stress on gelatin-$NaNbO_3$@PDMS constructs should remain below *ca.* 2.5 MPa to prevent scaffold densification, plastic deformation, and adverse effects on cell viability.

Additional data, such as density and mechanical properties during the first compression cycle at 50 % strain, are also summarized in **Table S1**.

*Mechano-electrical performance of scaffolds*

Determining the viscoelastic properties of scaffolds is crucial for mechanical compatibility with human tissues and predicting behavior under cyclic loading. During the first cycle, scaffolds with 18 % and 63 % porosity exhibit Young's moduli of 7–16 kPa (**Fig. 4a**), closely matching that of bone marrow in cancellous femoral bone (0.25–25 kPa) [41–43] and minimizing stress shielding. This alignment facilitates healthy bone remodeling under physiological loads and reduces the activation of osteoclast-mediated bone resorption, a common issue with overly rigid implants. Thus, it preserves bone density and maintains the long-term stability of the prosthetic interface, ensuring effective load distribution and minimizing the risk of stress shielding as per Wolff's Law.

This viscoelastic behavior is further clarified by examining the damping capacity (**Fig. 4b**). In the first cycle, the 63 % porosity scaffold dissipates the most energy—likely via heating—followed by the 0 % and 18 % porosity scaffolds. Despite initially dissipating more energy, the 63 % porosity scaffold shows lower stress resistance, indicating that it undergoes early permanent deformation, which reduces damping capacity

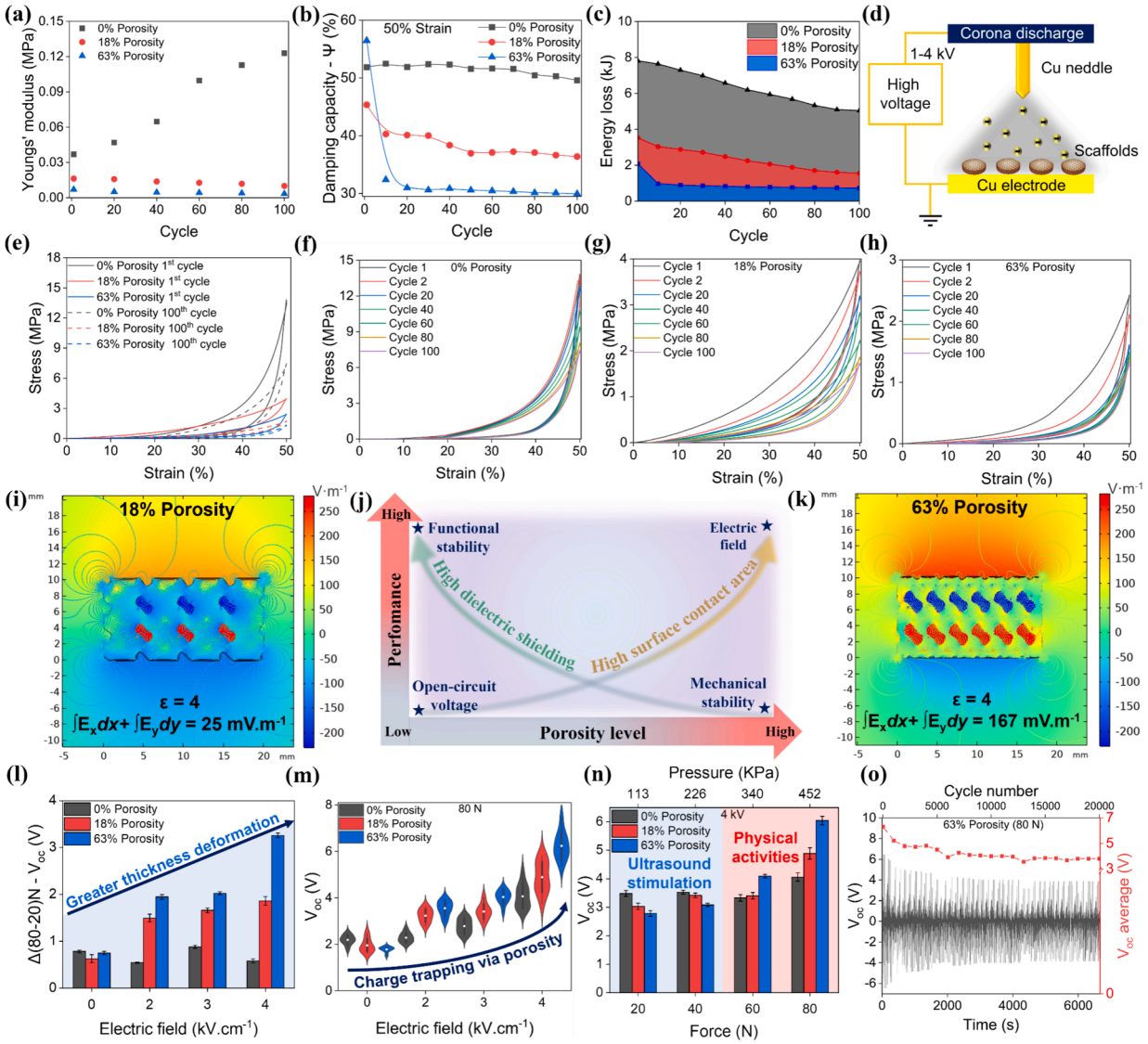


**Fig. 4.** Relationship between porosity levels and mechanical force triggers on the performance of mechano-electrical output and functional stability of electrically charged scaffolds. Cyclic mechanical tests on scaffolds with 0 %, 18 %, and 63 % porosity scaffolds over 100 cycles at strain 50 % yielding (a) Young's modulus, (b) damping capacity, and (c) energy loss. (d) A schematic illustration of corona discharge for electrically charged scaffolds, with an applied voltage difference between a needle and grid ranging from 1 to 4 kV. (e) Cyclic stress–strain curves at 1st and 100th cycles for scaffolds with 0 %, 18 %, and 63 % porosity scaffolds at 50 % strain. Sequential stress–strain curves in increments of 10 cycles over 100 cycles at 50 % strain for (f) 0 %, (g) 18 %, and (h) 63 % porosity scaffolds. Mind that Y-axes vary among the e-h charts, so please use care when comparing the profiles. COMSOL® simulations display electric field intensity and distribution for scaffolds with (i) 18 % and (k) 63 % porosity with a dielectric constant of 4 in aqueous media. The distribution of the electric potential along the X-axis within the scaffold and surrounding environment is displayed for each condition, while the integral of the electric field intensity along the X- and Y-axes ($\int E_x\,dx + \int E_y\,dy$) within all scaffold pores is described. (j) Conceptual diagram highlights the trade-off between porosity levels and scaffold performance, highlighting how effective contact surface area and dielectric shielding influence mechanical, electrical, and functional stabilities during stress. (l) Open-circuit voltage ($V_{oc}$) differences between 80 and 20 N force triggers across 1–4 kV·cm$^{-1}$ electric fields for scaffolds with 0, 18, and 63 % porosity, indicating a thickness-dependent output. (m) $V_{oc}$ output under an 80 N driving force across electric field polarization of 0, 2, 3, and 4 kV·cm$^{-1}$, indicating increased charge trapping capacity with higher pore levels in the scaffold. (n) $V_{oc}$ output under low- (≤300 kPa, e.g., US) and high-pressure triggers (>300 kPa, e.g., physical human activities) for scaffolds with 0 %, 18 %, and 63 % porosity polarized at 4 kV·cm$^{-1}$. (o) Long-term $V_{oc}$ functional stability of 63 % porosity scaffolds over 20,000 cycles under 80 N load.

and a diminished ability to recover its original form. This suggests that the 63 % porosity scaffold behaves more plastically at early cycles, quickly losing its energy dissipation capability due to permanent deformation. After the 20th cycle, the 63 % porosity scaffold behaves more elastically, with stable damping capacity until the 100th cycle.

Scaffolds with 0 % and 18 % porosities exhibited superior elastic behaviors, providing long-term durability and resistance to permanent deformation across multiple cycles. 0 % porosity scaffold demonstrates enhanced energy dissipation through absorption and conversion to heat or other non-recoverable forms, a critical property for bone scaffolds subjected to dynamic loads (e.g., walking, running, jumping), reducing implant damage and stress transfer to surrounding bone. However, because the 0 % porosity scaffold lacks macro-to-micro porosities, it limits cell adhesion and tissue integration. In contrast, the 18 % porosity scaffold combines significant damping capacity with elastic behavior, making it an effective choice for scaffolds designed to provide holistic mechanical and biological functionality.

The ability to dissipate energy as heat during cyclic loading reflects a balance between viscous (energy loss) and elastic (energy storage and recovery) properties. Energy dissipation stability inversely correlates with porosity: as porosity increases, both dissipation and stability decrease **(**Fig. 4**c)**. For instance, increasing porosity from 0 % to 18 % and 63 % reduces energy storage from 7.8 to 3.7 and 2.1 kJ, respectively, with dissipation capacity declining by 6 %, 13 %, and 56 % between the first and second cycles. These findings underscore the advantage of low porosity for energy absorption, making denser scaffolds better suited for load-bearing applications requiring effective cushioning and shock absorption.

Highly porous scaffolds (e.g., 63 %) exhibited reduced structural stability, increasing the risk of pore collapse and bone cell stress. To address this, mechanical stimulation was applied within the elastic region (<3 MPa) using US, thereby mitigating permanent deformation and minimizing artifacts that could compromise the interpretation of biological effects. This approach preserves scaffold integrity during stimulation and enables a more accurate evaluation of the scaffolds' stimuli-responsive behavior under US.

Cyclic mechanical testing across increasing strain (%) revealed the elastic regime and material densification associated with pore collapse, which could induce stress on bone cells (**Supplementary Fig. S3c-e)**. Densification occurred at ~ 40 % strain for the 0 % porosity scaffold, identified by a steep increase in stress slope, whereas gyroid scaffolds with 18 % and 63 % porosity exhibited delayed densification at *ca.* 45 % and ~ 49 % strain, respectively **(**Fig. 4**e)**.

Compressive stress curves from the 1st and 100th cycles reveal energy loss, absorption, and permanent plastic deformation, indicated by non-overlapping curves **(**Fig. 4**f-h)**. At 50 % strain, the 0 % porosity scaffold exhibits minimal curve decay, demonstrating high structural stability under cyclic loading **(**Fig. 4**f)**. Stability decreases with porosity, as shown by moderate decay in the 18 % porosity scaffold **(**Fig. 4**g)** and significant non-overlapping curves in the 63 % porosity scaffold **(**Fig. 4**h)**. These findings highlight a plastic-like response and greater structural collapse with increasing porosity.

To comprehend the electric field distribution and intensity within porous scaffolds, we conducted COMSOL simulations using the same physical and chemical parameters as the biological assessments **(**Fig. 4**i-k)**. From a biological perspective, the integrated electric field intensity across all pores is a more relevant measure than the average value, as biological outcomes depend on the entire scaffold volume. The total integrated electric field in the 63 % porous scaffold was approximately 6.7 times higher than in the 18 % porous scaffold under identical conditions, while the average electric field was about 350 % greater **(Supplementary Table S6)**. Thus, we further demonstrate that lower dielectric content (i.e., higher porosity) could be used to reduce the dielectric shielding effect, thereby enhancing electric field intensity within the pores.

To enhance responsiveness to stimuli and biological performance, electrically charged scaffolds were fabricated using corona discharge **(**Fig. 4**d)**, leveraging $NaNbO_3$ for its piezoelectric functionality. To better understand the range of scaffold applications in human implants, the pressure exerted on scaffolds during various human activities was categorized based on the electro-mechanical-structural relationship. Low-pressure conditions (≤300 kPa) correspond to activities with minimal mechanical impact, e.g., physiotherapy, US, and resting while lying down. In contrast, normal to high-pressure levels (>300 kPa) are associated with walking, standing, swimming, and sports, which induce greater mechanical stresses on scaffolds.

Two key dependencies of $V_{oc}$ behavior on mechanical tension regimes emerge, defined by a threshold pressure of approximately 300 kPa **(**Fig. 4**n)**. In the low-pressure regime (≤226 kPa), $V_{oc}$ decreases with increasing scaffold porosity, attributed to a reduced effective contact area that limits charge generation. Conversely, in the high-pressure regime (≥340 kPa), significant structural deformation enhances $V_{oc}$, driven by an increase in the effective contact surface area, especially in higher-porosity scaffolds that reduce compression resistance and facilitate X-deformation.

Given that the 63 % porosity scaffold represents the most mechanically unstable design, we evaluated its stimuli-responsive $V_{oc}$ stability over extended cycles under an 80-N (~452 kPa) load, representative of typical human mechanical triggers **(**Fig. 4**o)**. During the initial cycles (<1,000), $V_{oc}$ decreased significantly due to plastic deformation and electrode degradation, dropping from 6.3 to 3.8 V after 20,000 cycles before stabilizing with further cycling. These findings highlight the necessity of cyclic mechanical evaluations in scaffolds to identify stress–-strain ranges that preserve pore integrity under mechanical stimuli. Our results confirm that ultrasound is the most effective mechanical stimulus for assessing scaffold bioactivity.

These findings highlight the trade-off between porosity levels and scaffold performance in terms of mechanical, electrical, and functional stability, with surface area contact and dielectric shielding significantly influencing outcomes **(**Fig. 4**j)**. Higher porosity increases the integrated electric field intensity by reducing dielectric shielding, potentially boosting biological outcomes and recovery in functional activities. Additionally, the superior charge-trapping capability of the 63 % porous scaffold suggests that the actual electric field likely exceeds the theoretical values predicted by COMSOL. Conversely, reducing porosity enhances mechanical properties and functional stability by increasing material resistance and structural integrity. We established this trade-off to guide the design of advanced stimuli-responsive scaffolds, enabling fine-tuned structural optimization for specific mechanical, electrical, and biological outcomes.

The $V_{oc}$ differences observed between scaffolds at 80 and 20 N under 4 $kV{\cdot}cm^{-1}$ **(**Fig. 6**l)** highlight the structural impact of a 60-N load increase, particularly in higher-porosity scaffolds, which exhibit lower mechanical resistance and greater deformability. At low tension, the reduced $V_{oc}$ output in 63 % porosity scaffolds is attributed to their limited contact surface area compared to 0 % and 18 % porosity scaffolds, diminishing charge transfer efficiency. The increased charge capacity of higher-porosity scaffolds is demonstrated by the $V_{oc}$ improvement relative to non-polarized scaffolds (0 $kV{\cdot}cm^{-1}$), reaching 86 %, 150 %, and 240 % for porosities of 0 %, 18 %, and 63 % at 80 N, respectively **(**Fig. 4**m)**. This suggests that higher porosity creates additional charge traps within the scaffold, amplifying the electric field confined within the pores and potentially enhancing cell growth.

### *Ultrasonic Stimuli-Responsive effects on the biological performance of scaffolds*

Assessing biocompatibility is crucial before conducting biological tests to ensure materials do not harm cell viability or function. Our results confirmed the biocompatibility of $NaNbO_3$, showing that its incorporation into PDMS did not adversely affect cell viability, as indicated by live/dead staining **(Supplementary Fig. S7a-b)**. Metabolic

activity significantly increased from days 7 to 14 across all porosities and US conditions, demonstrating that the construct supports cell proliferation (Fig. 5**a**). US further enhanced metabolic activity, with more significant effects observed on day 14. The highest metabolic activity occurred in the 63 % porosity construct stimulated with 50 mW·cm$^{-2}$ at D14, suggesting this condition optimally promotes cellular activity. These findings indicate that cellular growth and proliferation are positively regulated by the electric field, supported by the highest electric field intensity (0.215 V·m$^{-1}$) observed in 63 % porosity scaffolds.

US upregulated calcium content compared to non-stimulated constructs, indicating that the mechano-electrical stimuli generated by US and electric field within the construct architecture promote osteogenic differentiation and mineralization, supporting bone tissue regeneration

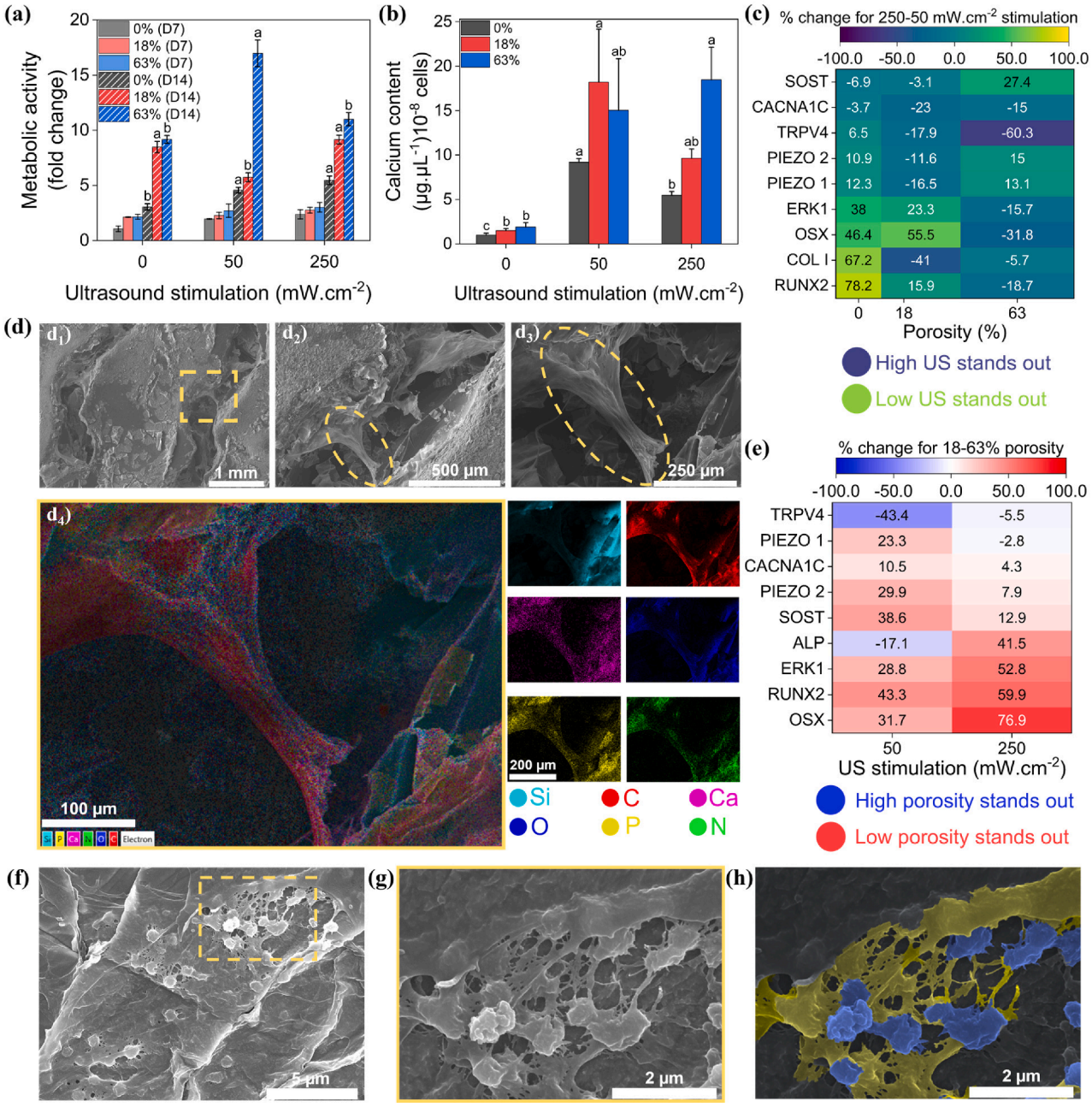


**Fig. 5.** Impact of ultrasound stimulation (US) and scaffold porosity on cell activity, calcium deposition, gene expression, and cell morphology. (a) Metabolic activity (fold change) and (b) calcium content in constructs with varying porosities (0 %, 18 %, and 63 %) under different US intensities (0, 50, and 250 mW·cm$^{-2}$) at 7 (D7) and 14 d (D14). Data are reported as mean values with errors (n = 4). Mean values followed by different superscript letters differ significantly (*p < 0.05) with comparisons of the same porosity levels and between US treatment groups at D14. (c) Heatmap showing the percentage change in gene expression markers (%) resulting from the difference between 250–50 mW·cm$^{-2}$ US for constructs with varying porosity (0 %, 18 %, and 63 %). (d) SEM images of 18 % porosity construct with 50 mW·cm$^{-2}$ US after 14 d, showing zoomed-in sections detailing cell growth through the pores at $d_1$) 30x (scale bar = 1 mm), $d_2$) x100 (scale bar = 500 µm), and $d_3$) 250× magnification (scale bar = 200 µm), and $d_4$) chemical composition determined by energy-dispersive X-ray spectroscopy (scale bar = 100 µm). (e) Heatmap displaying the percentage change in gene expression markers (%) comparing 18 and 63 % porosity of construct under different US (50 and 250 mW·cm$^{-2}$). SEM images of 0 % porosity of construct without US after 14 d at (f) 7 k magnification (scale bar = 5 µm), (g) zoomed-in section highlighting cell nuclei at 20 k magnification (scale bar = 2 µm) and (h) corresponding digitally colored image showing the cytoskeleton (yellow) and nuclei (blue) of cells at 20 k magnification (scale bar = 2 µm). (For interpretation of the references to colour in this figure legend, the reader is referred to the web version of this article.)

processes (Fig. 5**b**). This effect is associated with enhanced expression of osteogenic markers (*RUNX2*, *OSX*) under mild stimulation conditions, with the most significant improvements observed at 50 mW·cm$^{-2}$ US for the 63 % porosity scaffold and 250 mW·cm$^{-2}$ US for the 18 % porosity scaffold (Fig. 5**a-b**). These findings suggest the presence of an optimal US and electric field intensity, as higher US levels (250 mW·cm$^{-2}$) in 63 % porosity scaffolds may lead to overstimulation. Notably, the significant increase in calcium content—up to 1200 % compared to unstimulated controls—observed in the 63 % porosity scaffold at 50 mW·cm$^{-2}$ US aligns with the upregulation of osteogenic markers such as *OSX*, which are directly associated with bone matrix formation and mineralization. This demonstrates the role of these conditions in enhancing calcium deposition, a key marker of bone tissue formation.

Fig. 5**d** shows cell morphology on the 18 % porosity construct at 50 mW·cm$^{-2}$, where cells align along bridge-like structures spanning the pores. EDS analysis of these structures confirmed the presence of calcium and phosphorus, indicating calcium phosphate deposition associated with cell-driven mineralization. Additional SEM images demonstrate cell growth and spreading on 18 % and 63 % porosity constructs under 0, 50, and 250 mW·cm$^{-2}$ US (**Supplementary Fig. S9a-f**). Raman mapping further verified the presence of calcium phosphate, with characteristic peaks at *ca.* 600 cm$^{-1}$ (P-O-P bending), *ca.* 970 cm$^{-1}$ (phosphate ($PO_4^{3-}$) symmetric stretching), and 1045 cm$^{-1}$ (P-O asymmetric stretching) (**Supplementary Fig. S10a-d**) [44]. In contrast, the 0 % porosity construct exhibited reduced cell spreading, with prominent nuclei suggesting limited attachment due to the absence of pores and decreased surface area (Fig. 5**f-h**). These findings highlight the role of porosity in enhancing cell spreading and stretching, as observed in SEM images of porous constructs, through increased cell-surface interactions under both low and high US conditions.

Our findings show that 0 % porosity constructs exhibit higher gene expression for all markers at higher US (250 mW·cm$^{-2}$) compared to lower intensity (50 mW·cm$^{-2}$), except for the *ALP* marker and negligible difference in *CACNA1C* expression (**Supplementary Fig. S8a-h**). This highlights that increasing US effectively activates mechanosensitive pathways in non-porous constructs, leading to the upregulation of osteogenesis-related genes. The elevated *RUNX2* activity at 250 mW·cm$^{-2}$ further supports this, likely due to stronger activation of mechanosensitive pathways that enhance osteogenic signaling.

The focus of our stimuli-responsive scaffolds was to evaluate the effects of low (50 mW·cm$^{-2}$) and high (250 mW·cm$^{-2}$) US intensities, as well as low (18 %) and high (63 %) porosity in constructs, on gene expression markers. To ensure a fair comparison, we calculated the percentage change in gene expression by subtracting values for 50 from 250 mW·cm$^{-2}$ US for each porosity construct (0 %, 18 %, and 63 %) and normalized them to 250 mW·cm$^{-2}$ US at the corresponding porosity. To examine the impact of porosity, we subtracted values for 18 from 63 % porosity under the same US intensity (50 or 250 mW·cm$^{-2}$) and normalized them to 50 mW·cm$^{-2}$ US for the respective porosity. This data processing method highlights the percentage differences in gene expression, allowing a clear comparison of treatment conditions. Additionally, absolute values without normalization or comparisons are provided in **Supplementary Fig. S8a-h**. Heatmaps in Fig. 5**c** depict percentage changes in gene expression based on differences between 250 and 50 mW·cm$^{-2}$ US across porosity constructs, while Fig. 5**e** presents heatmaps comparing percentage changes between 18 % and 63 % porosity constructs under 50 and 250 mW·cm$^{-2}$ US.

The higher metabolic activity of the 63 % porosity construct compared to the 18 % construct at 50 mW·cm$^{-2}$ is further supported by ion channel activation mechanisms (*TRPV4* marker), showing a 60 % improvement over the 18 % porosity construct (Fig. 5**c**). This suggests that increased porosity and higher US intensity reduce the activity of voltage-gated calcium channels, which, due to overstimulation, may impair cellular processes involved in early osteogenesis and mechanotransduction. Furthermore, at high US intensity, *RUNX2* expression decreases with increasing porosity, indicating reduced early osteogenic differentiation (**Supplementary Fig. S8e**).

These results are likely explained by excessive US, which amplifies the electric field intensity within the pores as porosity increases, leading to cellular overstimulation. This effect also accounts for the reduced metabolic activity of the 63 % porosity construct when US is increased from 50 to 250 mW·cm$^{-2}$. Conversely, at 18 % porosity, increasing US from 50 to 250 mW·cm$^{-2}$ significantly upregulates the osteogenic transcription factor *OSX*, with a 55.5 % increase, indicating enhanced osteogenic differentiation likely driven by mechanotransduction pathways. An optimal electric field strength appears to be achieved within an intermediate US intensity range of 50 to 250 mW·cm$^{-2}$, depending on scaffold porosity. This is supported by the upregulation of gene expression at 250 mW·cm$^{-2}$ in low-porosity constructs, whereas higher porosity constructs favor upregulation at 50 mW·cm$^{-2}$ (Fig. 5**e**).

The most significant changes in gene expression induced by US and porosity are observed in *ALP* and *COL I* (**Supplementary Fig. S8i**). *ALP* expression consistently increases with pore level at 50 mW·cm$^{-2}$, peaking at intermediate electric field intensity. However, in the 63 % porosity construct at 250 mW·cm$^{-2}$, *ALP* expression decreases, likely due to electrical overstimulation, suggesting that higher US intensity shifts cells toward later differentiation stages. Similarly, *COL I* expression is highest in the 63 % porosity construct at 50 mW·cm$^{-2}$, with a steady decrease as pore level increases under higher US, further confirming the optimal range for electric stimulation.

To investigate the molecular mechanisms underlying osteogenic differentiation induced by zero-curvature geometries and ultrasound-triggered electromechanical stimulation, we analyzed key signaling markers associated with mechanotransduction and bone formation. Specifically, we quantified the gene expression levels of ERK1, a central mediator in the MAPK pathway [45,46], and SOST, a negative regulator of Wnt/β-catenin and YAP/TAZ signalling [47–51]. RT-qPCR analysis revealed that ERK1 expression was significantly upregulated in 18 % porous scaffolds under higher ultrasound intensity (250 mW·cm$^{-2}$), while decreased in 63 % porous scaffolds under the same conditions (Fig. 5**c,e and S8i**). This trend was consistent with the upregulation of downstream osteogenic transcription factors RUNX2 and OSX, suggesting that optimal ERK1 activation occurs at intermediate porosity and US conditions [52,53]. In parallel, SOST expression was reduced in both 18 % and 63 % porous scaffolds compared to the non-porous group, with the lowest levels observed in the 63 % porosity condition under low-intensity US (Fig. 5**c,e and S8j**). These findings support a model in which scaffold architecture and US-driven piezoelectric activation synergistically modulate electromechanical signaling, enhancing osteogenic pathways through ERK1 activation and SOST suppression. Together, this mechanistic insight complements our biological assessments and underscores the importance of scaffold design and dynamic stimulation in promoting bone regeneration.

Furthermore, we confirmed the positive influence of the electric field and US on cell alignment through qualitative DAPI/F-actin confocal imaging (Fig. 6**a–i**) and quantitative degree-based cell counting (Fig. 6**j–l**). To investigate this effect in detail, we analyzed the distribution and intensity of cell alignment based on cytoskeleton orientation, including accumulated cell counts within degree ranges of 1, 3, 5, 7, and 10° across 0–180° (**Supplementary Fig. S11a–l**).

Table 1 further highlights cell alignment peaks (%) within these ranges, showing a consistent increase in cell accumulation at 63 % porosity under 250 mW·cm$^{-2}$ US. To avoid overestimation and maintain accuracy, we used a three-degree range for constructing polar plots for each condition (Fig. 6**j–l**). Compared to unstimulated controls, US improved cell alignment by *ca.* 10 % with just 3 min of exposure every other day over a 14-d period, underscoring its significant potential as a physiotherapeutic strategy to enhance bone anisotropy and accelerate biological recovery.

Higher US (250 mW·cm$^{-2}$) markedly enhanced cell alignment across all porosities, with the strongest effect observed in the 63 % porosity construct, achieving approximately 14.2 % alignment. In contrast, at the

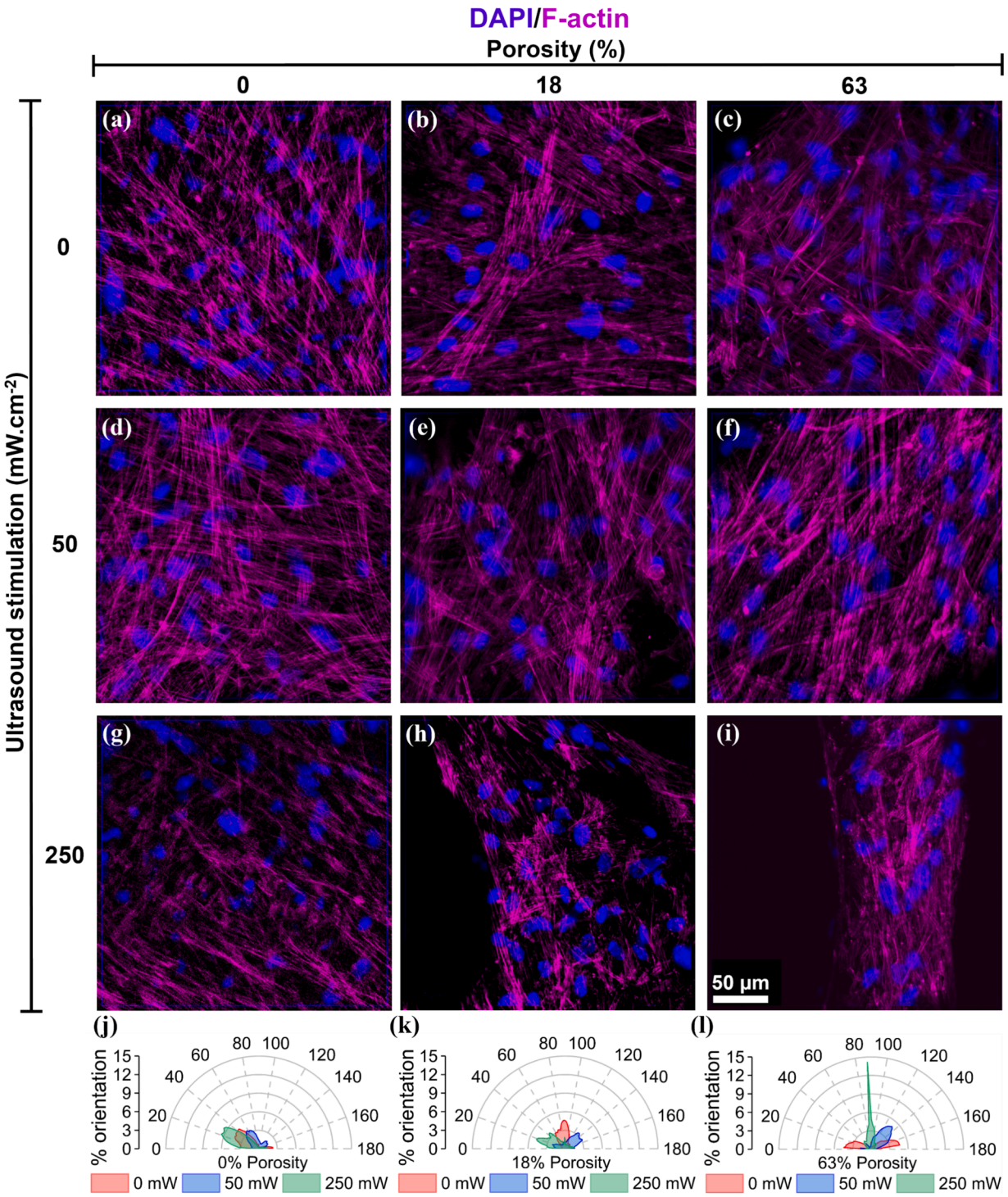


**Fig. 6.** Influence of ultrasound stimulation (US) and construct porosity on cellular alignment and actin filament organization. DAPI/F-actin confocal images of constructs under US at 0 mW·cm$^{-2}$ for (a) 0 %, (b) 18 %, (c) 63 % porosity; at 50 mW·cm$^{-2}$ for (d) 0 %, (e) 18 %, (f) 63 % porosity; and at 250 mW·cm$^{-2}$ for (g) 0 % (h), 18 % (i), 63 % porosity. Scale bar = 50 µm (applies to all images). Polar plots quantify cell alignment for (j) 0 %, (k) 18 %, and (l) 63 % porosity using three-degree accumulation range under each US condition (0, 50, and 250 mW·cm$^{-2}$). Cytoskeleton (F-actin, magenta) and nuclei (DAPI, blue) staining. (For interpretation of the references to colour in this figure legend, the reader is referred to the web version of this article.)

non-stimulated condition, cells exhibited reduced alignment (4.7 %) with dispersed nuclei and disorganized cytoskeletal structures. This suggests that the electric field intensity, modulated by US within the construct pores, promotes cytoskeletal alignment and contributes to bone anisotropy, which in turn supports daily mechanical loads while reducing the risk of injury. These findings underscore the synergistic effects of US and electric field intensity on cellular organization, offering insights into bone cell growth and advancing our understanding of tissue regeneration processes.

Although the gyroid structure was intentionally chosen to mimic trabecular bone microarchitecture rather than to impose strong directional steric guidance, the results suggest that further optimization of ultrasound parameters, e.g., intensity, duration, and frequency—could amplify alignment effects and potentially drive higher levels of

**Table 1**
Cell alignment (%) within accumulated degree ranges (1, 3, 5, 7, and 10°) for constructs with 0 %, 18 %, and 63 % porosity under ultrasound stimulation of 0, 50, and 250 mW·cm$^{-2}$.

| Construct porosity (%) | US (mW·cm$^{-2}$) | % Cell alignment by accumulated degree range | | | | |
|---|---|---|---|---|---|---|
| | | 1° | 3° | 5° | 7° | 10° |
| 0 | 0 | 1.5 | 4.5 | 7.5 | 10.3 | 14.8 |
| 0 | 50 | 1.2 | 3.4 | 5.7 | 7.9 | 11.2 |
| 0 | 250 | 2.2 | 6.6 | 10.8 | 14.7 | 21.2 |
| 18 | 0 | 1.6 | 4.6 | 7.6 | 10.7 | 15.1 |
| 18 | 50 | 1.1 | 3.4 | 5.5 | 7.8 | 10.3 |
| 18 | 250 | 1.7 | 4.9 | 8.0 | 11.1 | 15.3 |
| 63 | 0 | 1.6 | 4.7 | 7.7 | 10.6 | 15.2 |
| 63 | 50 | 3.4 | 4.9 | 6.7 | 8.4 | 16.3 |
| 63 | 250 | 6.4 | 14.2 | 17.3 | 20.4 | 24.2 |

anisotropy. In addition to mechanical modulation, future strategies could also explore surface functionalization with aligned biochemical cues or controlled electrochemical stimulation to further guide cellular orientation within 3D scaffolds. Together, these approaches highlight a promising avenue for future research using the precisely engineered scaffolds structures developed in this study, which can serve as a blueprint for advancing 3D scaffold fabrication and dynamic regenerative therapies.

## Conclusion

In this study, we synthesized a biocompatible piezoelectric compound ($NaNbO_3$), fabricated hierarchical porous scaffolds using sacrificial templating, and conducted mechano-electro characterization to advance stimuli-responsive biomaterials. We explored the effects of ultrasound stimulation on the biological performance of electrically charged scaffolds, focusing on the interplay between porosity, mechanical properties, and electric field intensity in promoting *in vitro* bone tissue formation. Corona discharge poling created electrically charged scaffolds, enhancing electric field intensity via charge trapping. Cyclic mechanical compression tests indicate the stress–strain range required to ensure the functional stability of scaffolds, demonstrating that ultrasonic stimulation effectively preserves pore integrity while delivering mechanical stimuli.

High-porosity scaffolds (63 %) showed increased electric field intensity due to the reduced dielectric shielding effect, significantly enhancing bioactivity. In contrast, low-porosity scaffolds (18 %) exhibited superior viscoelastic properties, ideal for load-bearing applications. The 63 % porous scaffolds synergized with US to enhance metabolic activity, mineralization, and gene expression, resulting in a 1200 % increase in calcium deposition. US also improved bone cell alignment by ~ 10 % with just 3 min exposures every other day over 14 d, demonstrating its potential to enhance bone anisotropy and biological recovery.

These findings advance the understanding of ultrasound stimuli in scaffolds mimicking cancellous bone architecture and highlight the potential of 3D sacrificial template methodologies for designing stimuli-responsive scaffolds. Our outcomes are expected to inspire future research to refine bone cell regeneration strategies by optimizing mechanical stimulation parameters—such as duration, power, and frequency—unlocking the full potential of ultrasound stimuli in advanced bioactive scaffolds for bone tissue engineering.

## Material and methods

*Materials:* Sylgard® 184 was purchased from Dow Corning® (Midland, MI, USA). Niobium (V) oxide ($Nb_2O_5$, 99.9 %) was acquired from Thermo Fisher Scientific® (Loughborough, UK). ABS light natural filament (1.75 mm) purchased from F3D (Novo Hamburgo, RS, Brazil). Sodium hydroxide (NaOH) pellets and type-A gelatin from porcine skin were purchased from Sigma-Aldrich Co. (St. Louis, MO, USA).

*Synthesis of $NaNbO_3$ nanocubes:* $NaNbO_3$ nanocubes were synthesized using a hydrothermal reactor with precise temperature control. The synthesis followed a modified procedure described by Jung et al. (Fig. 1**a)** [54]. To achieve phase purity and crystallinity, the nanoparticles were annealed at 600 °C for 12 h, yielding perovskite-phase $NaNbO_3$.

*3D printing of sacrificial ABS templates:* A temperature calibration tower was used to improve printability and shape consistency, resulting in 3D scaffolds with enhanced reproducibility **(**Supplementary Movie S3**)**. Sacrificial ABS templates were printed using a Sethi S3 FFF 3D printer (Campinas, Brazil) at 200–205 °C and a printing speed of 20 mm·s$^{-1}$. Three cylindrical templates, each 100 mm in diameter and height, were printed: one without internal patterns (*quasi*-0 % porosity) and two with gyroid-based structures exhibiting 35 % and 80 % porosity, respectively.

*Development of gyroid-structure scaffolds:* PDMS was prepared by mixing silicone elastomer and curing agent at a 10:1 wt ratio. $NaNbO_3$ (30 wt%) was incorporated, and the mixture was stirred for 20 min to ensure uniform dispersion. The resulting composite was poured into sacrificial ABS templates, vacuum-degassed for 1 h, and cured at 110 °C for 1 h. After curing, the ABS templates were dissolved in chloroform under magnetic stirring (450 rpm) overnight. The chloroform was replaced, and the process was repeated four times to ensure complete removal of the sacrificial templates. The $NaNbO_3$@PDMS scaffold was then washed three times with 70 % ethanol and ultrapure water to remove chloroform residues and dried at 70 °C for 6 h. The dried scaffolds were resized to 2.5 mm thickness and 8 mm diameter using a manual hollow punch. Finally, the scaffolds were coated with a 5 wt% gelatin solution (4 g of gelatin in 80 mL of deionized water) for 30 min and air-dried at room temperature [54,55].

*Electrical polarization by corona discharge:* Following the fabrication of the gelatin- $NaNbO_3$@PDMS scaffolds, the top and bottom surfaces were coated with gold/palladium (Au/Pd) via sputtering. While sputtering can theoretically coat all surfaces, the porous and sinuous geometry of the gyroid structure creates a "shadowing" effect, leaving internal surfaces largely uncoated and disrupting the formation of a continuous conductive path. Consequently, electrical connectivity is confined to the exposed external surfaces due to the line-of-sight nature of the sputtering process. Supplementary Movie S4 confirms the discontinuous conduction path between the top and bottom electrodes, effectively preventing short-circuiting and ensuring proper charge separation for measurable $V_{oc}$. The scaffolds were electrically polarized using corona discharge (custom-made machine), with electric fields of 2, 3, and 4 kV·cm$^{-1}$ applied at a current of ~ 3.7 μA for 40 min. Scaffolds without polarization (0 kV·cm$^{-1}$) served as controls to evaluate the efficiency of charge injection. A custom-built system was employed for the polarization process, utilizing a potential difference between a needle and a grounded grid positioned above the scaffold.

*Chemical, morphological, and compositional characterizations:* Various characterization techniques were employed throughout the scaffold manufacturing process to evaluate morphology, chemical properties, and composition. X-ray diffraction (XRD; Rigaku Ultima IV) was used to confirm the synthesis of sodium niobate from the $Nb_2O_5$ precursor, identify the crystalline structure, and verify its transformation into the piezoelectric perovskite phase. The material was analyzed in powder form using CuKα radiation (λ = 1.5405 Å), with Bragg angles (2θ) ranging from 20° to 80° at a scanning speed of 1°·min$^{-1}$. The volume fraction of the perovskite phase was calculated based on the intensity ratio of the primary XRD peaks corresponding to the perovskite phase ($NaNbO_3$) and $Nb_2O_5$ [23], using Eq. (1).

$$Wt\%perovskite = \frac{I_{perov}}{I_{perov} + I_{Nb_2O_5}} \times 100 \quad (1)$$

where $I_{perov}$ and $I_{Nb2O5}$ represent the intensities of the strongest reflection peaks for the perovskite phase (110) and $Nb_2O_5$ (180), respectively.

Morphological analysis of the scaffolds was performed using a magnifying lens (Leica, DM2700 M) and field emission scanning electron microscopy (FESEM; Hitachi Regulus 8220). Elemental composition was analyzed via energy-dispersive X-ray spectroscopy (EDX; Oxford INCA Energy 350). Fourier-transform infrared (FTIR) spectroscopy was carried out on a Nicolet 6700 spectrometer (Thermo Nicolet 6700) with an ATR accessory featuring a diamond crystal. The scan range was 4000–500 $cm^{-1}$ with 64 scans and a spectral resolution of 4 $cm^{-1}$.

2D and 3D projections of the scaffolds were obtained using X-ray micro-computed tomography (X-ray μCT; SkyScan 1272, Belgium), with quantitative analysis and volume/surface rendering performed using the CT-Analyser software. Static water contact angles (CA) were measured with a DataPhysics OCA 15 Plus using the sessile drop method and 1 μL ultrapure water droplets. The CA was recorded over 60 s with one data point per second, analyzed using the SCA 20 software and the Laplace-Young approximation model, with at least three measurements per sample.

*Mechanical properties:* Cyclic compression tests were conducted using an Instron 5569 (5-kN load cell, 60 mm·$min^{-1}$ crosshead speed) over 100 cycles at 12.5–50 % strain (**Supplementary Fig. S3a**). Scaffolds (100 mm diameter, thickness) were evaluated for compressive stress, energy absorption, and elastic modulus. Young's modulus was determined via linear regression in the viscoelastic region using Hooke's law. Damping capacity (ψ) was assessed every 10 cycles as the ratio of energy loss to strain energy (Eq. (2). Densification strain was identified from stress-strain curves as a 50 % slope increase post-elastic region, refined using second-derivative analysis to pinpoint pore collapse. Structural stability was evaluated by Y-axis deformation over 100 cycles, simulating real-world mechanical forces. Thickness deformation (ΔY) was quantified using Eq. (2).

$$\Delta Y = \frac{Y_f - Y_i}{Y_i} \times 100 \quad (2)$$

where $\Delta Y$ represents the percentage of thickness deformation after 100 cycles, $Y_i$ is the initial thickness, and $Y_f$ is the thickness after 100 cycles of compressive stress at 25 % or 50 % strain.

*Mechano-electrical output:* Open circuit electrical voltage ($V_{oc}$) was measured on cylindrical scaffolds (8 mm in diameter and 2.5 mm in thickness) by applying mechanical tensions of 20, 40, 60, and 80 N at 2 Hz, using a custom-built device. The $V_{oc}$ was also characterized from US at 50 and 250 mW·$cm^{-2}$ under the bone cell growth conditions used in biological characterization. Carbon tape was used to connect the positive and ground electrodes, and measurements were recorded with a Tektronix TBS1000C oscilloscope with data collected at 625 samples per second (20 k points over a 30-s range). To evaluate structural stability, the $V_{oc}$ was monitored during prolonged mechanical cycling (up to 20,000 cycles) in the plastic region (80 N at 2 Hz), focusing on the most unstable scaffold (63 % porosity). Further methodological details are provided in the Supplementary Material.

*Finite elemental analysis:* COMSOL Multiphysics simulations were performed to examine the impact of varying porosity levels (0 %, 18 %, and 63 %) and structural design on the intensity and distribution of the electric field within the scaffold pores. 2D images obtained from X-ray μCT were used to accurately design the scaffold structures and pores. Additional simulations considered different media (air or aqueous) and dielectric constants ($\epsilon_r$ = 4, 8, and 25). The modeling parameters are detailed in **Supplementary Table S2**.

*Biological characterization:* The complete biochemical methodology and characterization, including all detailed experimental procedures and protocols, are provided in the **Supplementary Material**. All biological characterizations were conducted using cylindrical scaffolds (8 mm in diameter, 2.5 mm in thickness) treated with 4 kV·$cm^{-1}$ corona discharge for 40 min.

*Cell culture:* The human bone marrow-derived mesenchymal stem cells (hBM-MSCs) used in the following study were isolated from bone marrow aspirates (Male, 24) (obtained from Centro Clínico da GNR, Portugal) according to protocols established at Stem Cell Engineering Research Group, Institute for Bioengineering and Biosciences (iBB) at Instituto Superior Técnico (IST) [56]. The cells were preserved in liquid/vapor nitrogen tanks as part of the cell bank available at iBB-IST. All human samples were obtained from healthy donors after written informed consent according to Directive 2004/23/EC of the European Parliament and of the Council of 31 March 2004 on setting standards of quality and safety for the donation, procurement, testing, processing, preservation, storage, and distribution of human tissues and cells (Portuguese Law 22/2007, June 29), with the approval of the Ethics Committee of the respective clinical institution. Before conducting the cell culture assays, the isolated hBM-MSCs were expanded on tissue culture flasks (T-75 $cm^2$) using low-glucose Dulbecco's Modified Eagle Medium (DMEM) (ThermoFisher, Waltham, MA, USA) supplemented with 10 vol % fetal bovine serum (Gibco FBS) (ThermoFisher, Waltham, MA, USA) and 1 vol% antibiotic–antimycotic (ThermoFisher, Waltham, MA, USA). The cell culture media was replaced every 3–4 d. The cells were kept in an incubator at 37 °C and 5 % $CO_2$ in a humidified atmosphere. All the experiments were conducted using cells between passages P5 and P6.

*Scaffold Preparation and Sterilization:* The scaffolds were then sterilized by UV light exposure overnight. Afterward, the gelatin-$NaNbO_3$@PDMS with different porosities were transferred to ultra-low cell attachment 6- and 24-well plates (Corning, Somerville, MA, USA), with the former being used for scaffolds under US and the latter being used for the respective static conditions. The scaffolds were then washed twice with a 70 vol% ethanol solution and three times with a 1 vol% anti-anti solution (prepared in PBS). Before cell seeding, the scaffolds were incubated in cell culture media for 1 h at 37 °C.

*Cell seeding, culture, and osteogenic differentiation:* Previously expanded hBM-MSCs were seeded in the gelatin-$NaNbO_3$@PDMS scaffolds at a density of 120.000 cells per construct. The cell-seeded scaffolds were incubated without cell culture media at 37 °C and 5 % $CO_2$ in a humidified atmosphere for 2 h to promote initial cell adhesion. Osteogenic media comprised of DMEM supplemented with 10 vol% FBS (MSC qualified), 10 mM of β-glycerolphosphate (Sigma-Aldrich, St. Louis, MI, USA), 10 nM of dexamethasone (Sigma-Aldrich), 50 μg·$mL^{-1}$ of ascorbic acid (Sigma-Aldrich) and 1 vol% anti-anti was added to the cell-seeded scaffolds. Media were renewed every 3–4 d. Cells was cultured for 14 d at 37 °C and 5 % $CO_2$ in a humidified atmosphere.

*Ultrasound stimulation (US):* US was applied using a SP300 ultrasound generator (Sonidel, Dublin, Ireland) with a 7 $cm^2$ ultrasonic probe in pulsed mode. Two stimulation regimens were tested: US intensities of 50 and 250 mW·$cm^{-2}$, at a frequency of 1 MHz, pulse repetition frequency (PRF) of 1 kHz, and a 20 % duty cycle. These were compared to a non-stimulated control. Constructs were stimulated for 3 min every two days over a 14-d culture period. Fig. 1**b,c** illustrates the US methodology for scaffolds with porosities of 0 %, 18 %, and 63 % at 0, 50, and 250 mW·$cm^{-2}$ intensities, as well as the experimental timeline from scaffold seeding on day 0.

*hBM-MSC metabolic activity assay:* The metabolic activity of human bone marrow-derived mesenchymal stem cells (hBM-MSCs) cultured on the scaffolds was assessed using an AlamarBlue™ assay (AlamarBlue™ Cell Viability Reagent; ThermoFisher) according to the manufacturer's guidelines. This non-destructive assay was performed under both static and mechanically stimulated experimental conditions on days 1, 7, and 14 of culture to evaluate cellular responses over time. A 10 vol% AlamarBlue™ solution prepared in cell culture media was added to the scaffolds, which were incubated at 37 °C in a humidified atmosphere with 5 % $CO_2$, protected from light, for 3 h. Fluorescence intensity was measured using a microplate reader (Infinite 200 Pro; Tecan, Zurich, Switzerland) at an excitation/emission wavelength of 560/590 nm. For each experimental group, measurements were obtained from three

independent scaffolds (n = 3), with fluorescence intensity recorded in triplicates per sample. Acellular scaffolds served as blank controls.

*Cell morphology via SEM and confocal microscopy:* SEM imaging (FESEM, Hitachi Regulus 8220) was used to analyze cell morphology after 14 d of culture, while the elemental composition was examined using energy-dispersive X-ray spectroscopy (EDX; Oxford INCA Energy 350). Samples were fixed, dehydrated, air-dried, and coated with gold/palladium before imaging. Additionally, DAPI and Phalloidin staining were used to visualize the nuclei and cytoskeleton of MSCs using confocal microscopy.

*Calcium Content and Mineralization:* Calcium deposition after 14 d of osteogenic differentiation was evaluated using a calcium colorimetric assay. Absorbance was measured following reaction with a chromogenic reagent and buffer, normalized to cell numbers. Mineralization on the gelatin-$NaNbO_3$@PDMS scaffolds was assessed using Raman spectroscopy after 14 d of cell culture. Spectral analysis focused on the 400–1200 $cm^{-1}$ range to detect calcium phosphate production, with Raman mapping at 600, 970, and 1045 $cm^{-1}$ conducted using an inVia™ Qontor confocal Raman microscope. A 532 nm laser at 50 % power, 1800 lines·$mm^{-1}$ grating, and a 50x objective lens were used for the measurements.

*Immunofluorescence of ECM proteins:* The production of type I collagen and osteopontin, key bone ECM proteins, by differentiated MSCs on the constructs, was assessed after 14 d using immunofluorescence imaging. Constructs fixed with PFA were washed with PBS and then treated with a 1 % BSA solution in PBS. Subsequently, cell-seeded gelatin-$NaNbO_3$@PDMS constructs were immersed in a permeabilization/blocking solution (1 % BSA, 10 % FBS, and 0.3 % Triton X-100) for 45 min at room temperature. Samples were then incubated overnight at 4 °C with primary antibodies for type I collagen (MA1-26771; ThermoFisher) and osteopontin (ab8448; Abcam) at a 1:250 dilutions in the blocking solution. The next day, constructs were treated with secondary antibodies (1:250 in 1 % BSA) for 1 h at room temperature in the dark: AlexaFluorTM 448 (ThermoFisher) for osteopontin and AlexaFluorTM 546 (ThermoFisher) for type I collagen. After two PBS washes, constructs were counterstained with DAPI (1.5 μg·$mL^{-1}$ in PBS) for 10 min, rinsed with PBS, and visualized under a 20x lens on a Zeiss Axio Imager Z2m confocal microscope.

*RNA isolation and qRT-PCR analysis:* Total RNA extraction was performed using the RNeasy Mini Kit (Qiagen, Hilden, Germany) on MSC-seeded gelatin-$NaNbO_3$@PDMS scaffolds after 14 d of osteogenic differentiation. Briefly, lysis buffer (RLT buffer) was added to each scaffold sample and agitated for 1 h. Total RNA was then isolated and purified according to the manufacturer's instructions. RNA concentration was measured using a NanoVue Plus spectrophotometer (GE Healthcare, Chicago, IL, USA). Complementary DNA (cDNA) was synthesized from the purified RNA using the High-Capacity cDNA Reverse Transcription Kit (Applied Biosystems, Waltham, MA, USA), following the manufacturer's protocol. Reaction mixtures were incubated in a T100™ thermal cycler (Bio-Rad, Hercules, CA, USA) at 25 °C for 10 min, 37 °C for 120 min, and 85 °C for 5 min, before being held at 4 °C until further use. Primer sequences for the qRT-PCR analysis are listed in **Supplementary Table S2**. Relative gene expression was calculated using the $2^{-\Delta\Delta Ct}$ method (n = 3).

A heatmap was generated to visualize gene expression changes under varying US intensities and scaffold porosities. To quantify the effect of US, the percentage change in gene expression between 250 and 50 mW·$cm^{-2}$ was calculated for each porosity condition (0 %, 18 %, and 63 %), normalized to the expression at 250 mW·$cm^{-2}$. For porosity comparisons, the percentage change in gene expression between 18 % and 63 % porosity was calculated for each US intensity (50 and 250 mW·$cm^{-2}$), relative to the expression at 18 % porosity. These percentage differences were then used to construct a standardized heatmap on a 200 % scale, featuring 10 major and 20 minor gradient levels for detailed visualization.

*Statistical Analyses:* Data are presented as mean values with the standard error of independent measurements or assays (n ≥ 3). Statistical analysis was performed using the OriginPro 8.5 and Minitab 17 softwares. Quantitative data were subjected to analysis of variance (ANOVA), followed by Tukey's mean comparison test. P-values of $< 0.05$ were considered significant for all statistical tests, where applicable.

## CRediT authorship contribution statement

**Rafael R.A. Silva:** Writing – review & editing, Methodology, Investigation, Data curation. **Frederico Barbosa:** Writing – review & editing, Methodology, Investigation, Formal analysis. **Guilherme Ferreira:** Writing – review & editing, Methodology, Investigation, Formal analysis. **Carlos Ureña:** Writing – review & editing, Methodology, Investigation, Formal analysis. **Eduardo H. Backes:** Writing – review & editing, Data curation, Conceptualization. **José M. Inácio:** Writing – review & editing, Methodology, Investigation, Formal analysis. **José A. Belo:** Writing – review & editing, Methodology, Investigation, Formal analysis. **Rui Igreja:** Writing – review & editing, Methodology, Investigation, Formal analysis. **João C. Silva:** Writing – review & editing, Methodology, Investigation, Formal analysis. **Luiz H.C. Mattoso:** Supervision, Project administration, Funding acquisition, Data curation, Conceptualization. **Elvira Fortunato:** Writing – review & editing, Supervision, Project administration, Funding acquisition, Data curation, Conceptualization. **Henrique M.V. Almeida:** Writing – review & editing, Supervision, Methodology, Data curation, Conceptualization. **Rodrigo Martins:** Writing – review & editing, Supervision, Project administration, Funding acquisition, Conceptualization. **Caio G. Otoni:** Writing – review & editing, Supervision, Project administration, Funding acquisition, Conceptualization.

## Declaration of competing interest

The authors declare that they have no known competing financial interests or personal relationships that could have appeared to influence the work reported in this paper.

## Acknowledgements

We acknowledge the Coordenação de Aperfeiçoamento de Pessoal de Nível Superior - Brasil (CAPES) - Finance Code 001, the Brazilian National Council for Scientific and Technological Development (CNPq) (grants no. 304753/2022-0, 200337/2022-0, 402511/2022-0, and 406925/2022-4), the São Paulo Research Foundation (FAPESP) (grant no. 2021/12071-6), FINEP (MATENERGIA, grant no. 01.22.0177), and the Graduate Program in Materials Science and Engineering, Federal University of Sao Carlos (PPGCEM/UFSCar). This work was also financed by national funds from FCT - Fundação para a Ciência e a Tecnologia, in the scope of the projects InSilico4OCReg (PTDC/EMESIS/0838/2021), LA/P/0037/2020, PhD scholarship (2022.10572.BD), UIDB/50025/2020 and the Associate Laboratory Institute of Nanostructures, Nanomodelling and Nanofabrication – i3N, iBB (UID/BIO/04565/2022), to the Associate Laboratory I4HB (LA/P/0140/2020), the Research Unit iNOVA4Health (UIDB/04462/2020 and UIDP/04462/2020) and the Associated Laboratory LS4FUTURE (LA/P/0087/2020). This work was also partially supported by European Union's Horizon 2020 Research and Innovation Programme under Grant Agreements number 952169 (SYNERGY, H2020-WIDESPREAD-2020-5, CSA) and 101008701 (EMERGE, H2020-INFRAIA-2020-1), and 101070255 (REFORM, HORIZON-CL4-2021-DIGITAL-EMERGING-01). We acknowledge Pedro Ivo Cunha Claro (UFSCar) for his support with data analysis.

## Appendix A. Supplementary data

Supplementary data to this article can be found online at https://doi.org/10.1016/j.mattod.2025.06.013.

## Data availability

Data will be made available on request.

## References


[1] R.K. Aaron, D.M.K. Ciombor, B.J. Simon, Clin. Orthop. Relat. Res. 419 (2004) 21.
[2] R.E. Brighton, C.T. Friedenberg, Z.B. Mitchell, E.I. Booth, Orthop. Relat. Res. 124 (1977) 106.
[3] C.T. Brighton, W. Wang, R. Seldes, G. Zhang, S. Pollack, J. Bone Jt. Surgery. Am. 83 (2001) 1514.
[4] B.M. Isaacson, R.D. Bloebaum, J. Biomed. Mater. Res. - Part A 95 (2010) 1270.
[5] M. Levin, Bioelectromagnetics 24 (2003) 295.
[6] J. Zhang, M. Li, E.T. Kang, K.G. Neoh, Acta Biomater. 32 (2016) 46.
[7] P. Moroder, M.B. Runge, H. Wang, T. Ruesink, L. Lu, R.J. Spinner, A.J. Windebank, M.J. Yaszemski, Acta Biomater. 7 (2011) 944.
[8] J. Tian, R. Shi, Z. Liu, H. Ouyang, M. Yu, C. Zhao, Y. Zou, D. Jiang, J. Zhang, Z. Li, Nano Energy 59 (2019) 705.
[9] M.N. Collins, G. Ren, K. Young, S. Pina, R.L. Reis, J.M. Oliveira, Adv. Funct. Mater. (2021) 31.
[10] C.N. Kelly, J. Francovich, S. Julmi, D. Safranski, R.E. Guldberg, H.J. Maier, K. Gall, Acta Biomater. 94 (2019) 610.
[11] S.B.G. Blanquer, M. Werner, M. Hannula, S. Sharifi, G.P.R. Lajoinie, D. Eglin, J. Hyttinen, A.A. Poot, D.W. Grijpma, Biofabrication (2017) 9.
[12] H. Montazerian, M.G.A. Mohamed, M.M. Montazeri, S. Kheiri, A.S. Milani, K. Kim, M. Hoorfar, Acta Biomater. 96 (2019) 149.
[13] S.D. Smith, D.A. Agard, R.J. Spontak, Adv. Mater. 14 (2002) 1615.
[14] S.J.P. Callens, D.C. Tourolle né Betts, R. Müller, A.A. Zadpoor, Acta Biomater. 130 (2021) 343.
[15] R.V. Chernozem, M.A. Surmeneva, S.N. Shkarina, K. Loza, M. Epple, M. Ulbricht, A. Cecilia, B. Krause, T. Baumbach, A.A. Abalymov, B.V. Parakhonskiy, A. G. Skirtach, R.A. Surmenev, ACS Appl. Mater. Interfaces 11 (2019) 19522.
[16] M.T. Arafat, C.X.F. Lam, A.K. Ekaputra, S.Y. Wong, X. Li, I. Gibson, Acta Biomater. 7 (2011) 809.
[17] K. Zheng, J. Wu, W. Li, D. Dippold, Y. Wan, A.R. Boccaccini, ACS Biomater. Sci. Eng. 4 (2018) 1546.
[18] S. Afewerki, A. Sheikhi, S. Kannan, S. Ahadian, A. Khademhosseini, Bioeng. Transl. Med. 4 (2019) 96.
[19] X. Li, J. Xie, X. Yuan, Y. Xia, Langmuir 24 (2008) 14145.
[20] T. Ibn-Mohammed, S.C.L. Koh, I.M. Reaney, A. Acquaye, D. Wang, S. Taylor, A. Genovese, Energy Environ. Sci. 9 (2016) 3495.
[21] T. Ibn-Mohammed, S.C.L. Koh, I.M. Reaney, D.C. Sinclair, K.B. Mustapha, A. Acquaye, D. Wang, MRS Commun. 7 (2017) 1.
[22] A. Sharma, U. Bhardwaj, D. Jain, H.S. Kushwaha, ACS Omega 7 (2022) 7595.
[23] A. Sharma, U. Bhardwaj, D. Jain, H.S. Kushwaha, iScience 25 (2022), 104915.
[24] N. Chaiyo, B. Boonchom, N. Vittayakorn, J. Mater. Sci. 45 (2010) 1443.
[25] G. Gouget, M. Duttine, E. Durand, A. Villesuzanne, V. Rodriguez, F. Adamietz, T. Le Mercier, M.D. Braida, A. Demourgues, ACS Appl. Electron. Mater. 1 (2019) 513.
[26] S. Li, Q. Xu, E. Uchaker, X. Cao, G. Cao, CrystEngComm 18 (2016) 2532.
[27] S.L. Fernandes, L.G.S. Albano, L.J. Affonço, J.H.D. da Silva, E. Longo, C.F. de O. Graeff, Front. Chem. 7 (2019) 1.
[28] U. Farooq, R. Phul, S.M. Alshehri, J. Ahmed, T. Ahmad, Sci. Rep. 9 (2019) 1.
[29] M. Boukriba, F. Sediri, N. Gharbi, Mater. Res. Bull. 48 (2013) 574.
[30] T.Y. Ke, H.A. Chen, H.S. Sheu, J.W. Yeh, H.N. Lin, C.Y. Lee, H.T. Chiu, J. Phys. Chem. C 112 (2008) 8827.
[31] S.K. Mohanty, B. Behera, B. Pati, P.R. Das, J. Mater. Sci. Mater. Electron. 29 (2018) 12269.
[32] M. Nyman, A. Tripathi, J. B. Parise, R. S. Maxwell, T. M. Nenoff, **2002**, 0.
[33] M.J. Hossan, M.A. Gafur, M. Kadir, M.M. Karim, Int. J. Eng. Technol. 14 (2014) 113.
[34] C. Wang, D. Xu, L. Lin, S. Li, W. Hou, Y. He, L. Sheng, C. Yi, X. Zhang, H. Li, Y. Li, W. Zhao, D. Yu, Mater. Sci. Eng. C (2021) 131.
[35] G. Li, L. Wang, W. Pan, F. Yang, W. Jiang, X. Wu, X. Kong, K. Dai, Y. Hao, Sci. Rep. 6 (2016) 1.
[36] J. Parthasarathy, B. Starly, S. Raman, A. Christensen, J. Mech. Behav. Biomed. Mater. 3 (2010) 249.
[37] J.A. Bouwstra, A. De Graaff, G.S. Gooris, J. Nijsse, J.W. Wiechers, A.C. Van Aelst, J. Invest. Dermatol. 120 (2003) 750.
[38] S. Chen, L. Li, C. Zhao, J. Zheng, Polymer (Guildf). 51 (2010) 5283.
[39] S.M. Mantila Roosa, J.M. Kemppainen, E.N. Moffitt, P.H. Krebsbach, S.J. Hollister, J. Biomed. Mater. Res. - Part A 92 (2010) 359.
[40] N. Abbasi, S. Hamlet, R.M. Love, N.T. Nguyen, J. Sci. Adv. Mater. Devices 5 (2020) 1.
[41] M.Q. Cheng, T. Wahafu, G.F. Jiang, W. Liu, Y.Q. Qiao, X.C. Peng, T. Cheng, X. L. Zhang, G. He, X.Y. Liu, Sci. Rep. 6 (2016) 1.
[42] D.E. Discher, D.J. Mooney, P.W. Zandstra, Science 324 (5935) (2009) 1673–1677.
[43] S.H. Parekh, K. Chatterjee, S. Lin-Gibson, N.M. Moore, M.T. Cicerone, M.F. Young, C.G. Simon, Biomaterials 32 (2011) 2256.
[44] L.E. Jansen, N.P. Birch, J.D. Schiffman, A.J. Crosby, S.R. Peyton, J. Mech. Behav. Biomed. Mater. 50 (2015) 299.
[45] J.A. Stammeier, B. Purgstaller, D. Hippler, V. Mavromatis, M. Dietzel, MethodsX 5 (2018) 1241.
[46] L. Leppik, K.M.C. Oliveira, M.B. Bhavsar, J.H. Barker, Eur. J. Trauma Emerg. Surg. 46 (2020) 231.
[47] D. Khare, B. Basu, A.K. Dubey, Biomaterials 258 (2020) 120280.
[48] B.C. Heng, X. Zhang, D. Aubel, Y. Bai, X. Li, Y. Wei, M. Fussenegger, X. Deng, Front. Cell. Dev. Biol. 8 (2020) 1.
[49] J.K. Virdi, P. Pethe, Tissue Eng. Regen. Med. 18 (2021) 199.
[50] L. Azzolin, T. Panciera, S. Soligo, E. Enzo, S. Bicciato, S. Dupont, S. Bresolin, C. Frasson, G. Basso, V. Guzzardo, A. Fassina, M. Cordenonsi, S. Piccolo, Cell 158 (2014) 157.
[51] A.A. Bertrand, S.H. Malapati, D.T. Yamaguchi, J.C. Lee, Adv. Healthc. Mater. (2020) 9.
[52] K.K. Das, B. Basu, P. Maiti, A.K. Dubey, Appl. Mater. Today 39 (2024) 102332.
[53] Y. Wu, J. Wu, X. Huang, X. Zhu, W. Zhi, J. Wang, D. Sun, X. Chen, X. Zhu, X. Zhang, Mater. Today Bio 23 (2023) 100891.
[54] J.H. Jung, M. Lee, J. Il Hong, Y. Ding, C.Y. Chen, L.J. Chou, Z.L. Wang, ACS Nano 5 (2011) 10041.
[55] A.L. Metze, A. Grimm, P. Nooeaid, J.A. Roether, J. Hum, P.J. Newby, D. W. Schubert, A.R. Boccaccini, Key Eng. Mater. 541 (2013) 31.
[56] M.S. Carvalho, L. Alves, I. Bogalho, J.M.S. Cabral, C.L. da Silva, Front. Cell. Dev. Biol. 9 (2021) 1.